crystals

MDPI

Review

Advances in Two-Dimensional Materials for Optoelectronics Applications

Mingyue Zhao [1], Yurui Hao [1], Chen Zhang [1], Rongli Zhai [1], Benqing Liu [1], Wencheng Liu [1], Cong Wang [1], Syed Hassan Mujtaba Jafri [2], Aamir Razaq [3], Raffaello Papadakis [4,5], Jiangwei Liu [6,*], Xiaoling Ye [1,*], Xiaoxiao Zheng [1,*] and Hu Li [1,7,8,*]

1 Shandong Technology Centre of Nanodevices and Integration, School of Microelectronics, Shandong University, Jinan 250101, China
2 Department of Electrical Engineering, Mirpur University of Science and Technology (MUST), Mirpur 10250, Azad Jammu and Kashmir, Pakistan
3 Department of Physics, COMSATS University Islamabad, Lahore Campus, Lahore 54000, Punjab, Pakistan
4 TdB Labs AB, Uppsala Business Park, 75450 Uppsala, Sweden
5 Department of Chemistry, Uppsala University, 75120 Uppsala, Sweden
6 School of Energy and Power Engineering, Shandong University, Jinan 250061, China
7 Shenzhen Research Institute, Shandong University, Shenzhen 518057, China
8 Department of Materials Science and Engineering, Uppsala University, 75121 Uppsala, Sweden
* Correspondence: jiangwei.liu@sdu.edu.cn (J.L.); 202112357@mail.sdu.edu.cn (X.Y.); 202120353@mail.sdu.edu.cn (X.Z.); hu.li@sdu.edu.cn (H.L.)

Abstract: The past one and a half decades have witnessed the tremendous progress of two-dimensional (2D) crystals, including graphene, transition-metal dichalcogenides, black phosphorus, MXenes, hexagonal boron nitride, etc., in a variety of fields. The key to their success is their unique structural, electrical, mechanical and optical properties. Herein, this paper gives a comprehensive summary on the recent advances in 2D materials for optoelectronic approaches with the emphasis on the morphology and structure, optical properties, synthesis methods, as well as detailed optoelectronic applications. Additionally, the challenges and perspectives in the current development of 2D materials are also summarized and indicated. Therefore, this review can provide a reference for further explorations and innovations of 2D material-based optoelectronics devices.

Keywords: two-dimensional materials; graphene; transition-metal dichalcogenides; optoelectronics

Citation: Zhao, M.; Hao, Y.; Zhang, C.; Zhai, R.; Liu, B.; Liu, W.; Wang, C.; Jafri, S.H.M.; Razaq, A.; Papadakis, R.; et al. Advances in Two-Dimensional Materials for Optoelectronics Applications. *Crystals* **2022**, *12*, 1087. https://doi.org/10.3390/cryst12081087

Academic Editor: Dmitri Donetski

Received: 30 June 2022
Accepted: 31 July 2022
Published: 4 August 2022

1. Introduction

Graphene, as a representative two-dimensional (2D) material, has attracted considerable attention since it was mechanically exfoliated from bulk graphite in 2004 [1]. Its special two-dimensional honeycomb lattice endows it with numerous excellent properties such as high carrier mobility, high mechanical strength, excellent optical transparency, and a wide absorption spectrum [2,3], which makes it exhibit great application potential in many areas [4]. The discovery and development of graphene has further stimulated research interests in other 2D materials.

Two-dimensional materials are layered crystalline solids that have strong bonding in the crystal plane, while the forces between the adjacent atomic layers are weak van-der-Waals forces [5–7]. The special structure of 2D materials endows them with many remarkable abilities. First, quantum confinement in the direction perpendicular to the 2D plane introduces some novel optical and electronic performances to 2D materials, which are distinct from their bulk parent materials [8]. Second, the surfaces of these materials are naturally passivated and they have no dangling bond, which facilitates the integration of 2D materials with photonic structures [8,9]. In addition, using diverse 2D materials can build vertical heterostructures, in which the different layers are bonded by van der Waals forces, averting the issue of lattice mismatch. Third, a host of 2D materials can interact strongly

with light [10]. For instance, monolayer MoS_2 can absorb nearly 10% of perpendicular incident light at excitonic resonances [11]. Finally, 2D materials can cover a broad range of electromagnetic spectra due to their different electronic properties [12]. Due to their special properties, 2D materials show great application potential in various fields, especially in optoelectronics applications [13–15]. For example, graphene has become a potential candidate in the applications of light modulation, detection and manipulation because it can interact with light in a wide range of spectra. Some transition metal dichalcogenides (TMDCs) such as MoS_2 and WS_2 have sizable bandgaps and possess illustrious light-emitting performances, ensuring their applications in photodetectors, transistors, and other optoelectronics devices [8,16]. Hexagonal boron nitride (hBN) is also a significant 2D material and it is often used as an outstanding dielectric on account of its large bandgap. Furthermore, it can be incorporated into heterostructures to act as the electrostatic gating of other 2D materials. In this paper, we give a comprehensive review of the structure, properties, and optical applications of 2D materials. We also make an outlook of the prospects of 2D materials.

2. Graphene

2.1. Structure and Optical Property

2.1.1. Morphology and Structure

Graphene is made up of a single layer of carbon atoms which is arranged in a honeycomb lattice. The real-space images of the atomic lattice of monolayer graphene were obtained and used to characterize the thicknesses and nanoscale corrugation of a clean graphene sheet devoid of any impurities in 2007 [17,18]. The sp^2 hybridization between one s orbital and two p orbitals leads to a planar structure with the formation of a bond between carbon atoms that are separated by 1.42 Å. Due to the Pauli principle, these bands have a filled shell and, hence, form a deep valence band. The unaffected p orbital, which is perpendicular to the planar structure, can bind covalently with neighboring carbon atoms, leading to the formation of a π band. Since each p orbital has one extra electron, the π band is half filled.

As is well-known, graphene is a zero bandgap semi-metal material, because its conduction band and valence band intersect at the Dirac point. The energy band structure satisfies the Dirac equation, unlike traditional metals or semiconductors that satisfy the Schrödinger equation. At the K point, the energy of the electron is linearly related to its momentum, the static effective mass of the electron is 0, and the behavior is similar to that of a photon [19].

2.1.2. Optical Properties

Graphene has excellent light transmittance, with a light transmittance of 97.7% for light with a wavelength of 400–800 nm. Electrons in graphene behave as massless two-dimensional particles, which leads to a significant wavelength-independent absorption ($\pi a < 2.3\%$ in the infrared limit, where a is the fine structure constant) for normal incident light below about 3 eV [20]. The number of graphene layers is linearly related with the light transmittance [21]. As the number of layers increases, the light transmittance decreases, making it possible to roughly judge the number of graphene layers by an optical microscope [8]. Mono- and bi-layer graphene becomes completely transparent when the optical energy is smaller than that which is double the Fermi level, owing to Pauli blocking [22], and these properties would suit many controllable photonic devices.

The high-frequency conductivity for Dirac fermions in graphene has been considered as a constant ($\pi e^2/2h$) [22,23], from the infrared to the visible range of the spectrum. Graphene has good anti-reflection properties, and its reflectivity is less than 0.1% when the light is incident perpendicular to the graphene surface. In addition, graphene also has good nonlinear optical properties. When the electric field generated by the incident light resonates with the outermost electrons of the carbon atoms in graphene, the electron cloud in graphene shifts and generates polarization, so graphene can exhibit nonlinear

optical properties such as saturable absorption [24], the Kerr effect [25,26], and two-photon absorption [27]. Therefore, graphene has application potential in many optical fields such as ultrafast photonics [28].

2.2. Production Methods

The integration of novel materials can bring a new dimension to future technologies; therefore, large-scale and cost-effective production methods are necessary. Up to now, the main approaches to produce graphene are shown in Figure 1. These preparation methods can be roughly divided into two categories: one is the "top-down" synthesis method—that is, the desired nanoscale graphene is prepared from large-scale graphite by various techniques, such as mechanical exfoliation, the liquid-phase ultrasonic exfoliation method and the arc method [13]; the other is the "bottom-up" synthesis method—that is, small carbon-containing structural units are self-assembled into graphene through interaction, such as chemical vapor deposition [29].

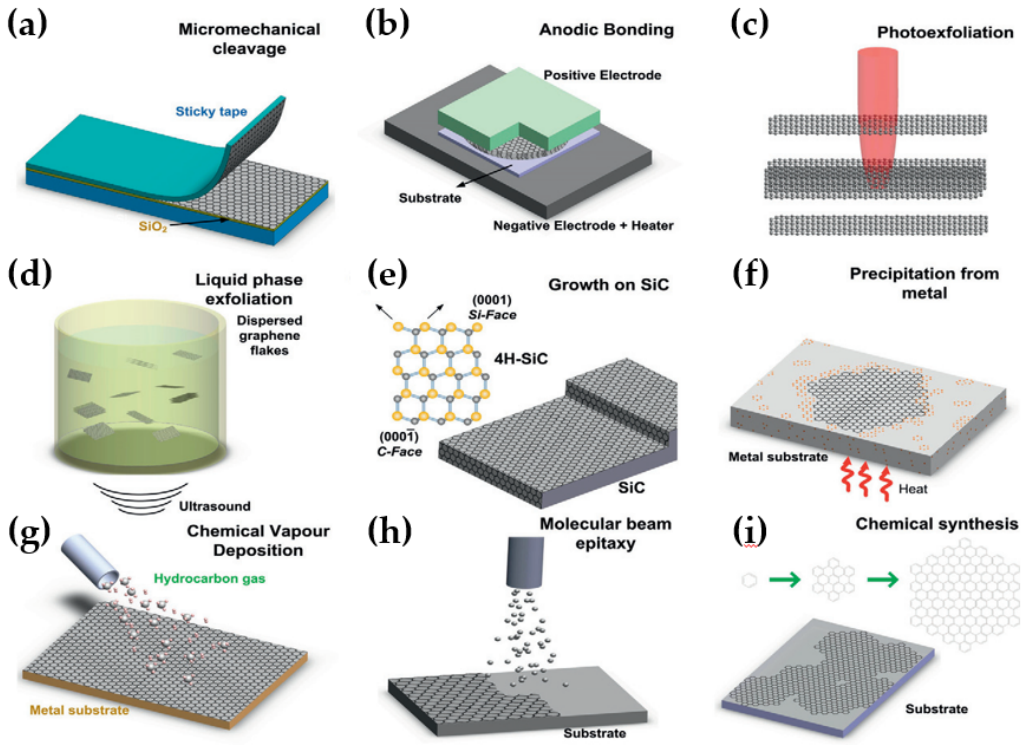

Figure 1. Schematic illustration of the main graphene production techniques. (**a**) Micromechanical cleavage. (**b**) Anodic bonding. (**c**) Photoexfoliation. (**d**) Liquid phase exfoliation. (**e**) Growth on SiC. Gold and grey spheres represent Si and C atoms, respectively. At elevated T, Si atoms evaporate (arrows), leaving a carbon-rich surface that forms graphene sheets. (**f**) Segregation/precipitation from carbon containing metal substrate. (**g**) Chemical vapor deposition. (**h**) Molecular Beam epitaxy. (**i**) Chemical synthesis using benzene as building block (Reproduced with permission from ref. [30]. Copyright 2012 Elsevier Publications).

2.3. Optical Applications

Due to the unique electrical and optical properties, including ultra-high carrier mobility, ultra-strong ballistic transport effect, ultra-fast optical response time, and ultra-wide spectral response range, graphene has considerable potential for optoelectronics applications. In this section, we review the optical applications of graphene in photodetectors, organic solar cells, electromagnetic optical nanoantennas, and so on, which are summarized in Table 1.

Table 1. Optoelectronic applications based on graphene.

Applications	Materials	Photoresponsivity		Ref.
Photodetectors	Graphene/WS_2/graphene	121 A W^{-1} (at 532 nm)		[31]
	Carbon nanotube/graphene	1.48×10^5 A W^{-1} (at 1550 nm)		[32]
	Graphene/PbS quantum dots	10^7 A W^{-1} (at 635 nm)		[33]
	Materials	**Power conversion efficiency**	**Optical transmittance**	**Ref.**
Organic solar cells	Polyimide/graphene	15.2%	92%	[34]
	AZO/graphene/Cu/AZO	4.63%	82%	[35]
	Materials	**Operating frequency**	**Gain**	**Ref.**
Electromagnetic optical nanoantennas	Graphene-based nano-antenna	55 THz	5.47 dB	[36]
	Graphene based slotted bowtie optical plasmonic nanoantenna	193.5 THz	7.38 dB	[37]
	Materials	**Modulation depth**	**Bandwidth**	**Ref.**
Optoelectronic modulators	Double-layer graphene/double rectangle metal nanoribbons	3.12 dB μm^{-1}	380.23 GHz	[38]
	Graphene/hBN	14–20 dB μm^{-1}	-	[39]

2.3.1. Photodetectors

Photodetectors refer to devices that can convert optical signals into electrical signals, involving three physical processes, namely light capture, exciton separation, and charge transfer to electrodes. The zero bandgap electronic structure of graphene gives the graphene photodetectors broadband detection properties and an extremely fast response speed compared with other detectors [40]. However, this characteristic of graphene also makes the exciton recombination rate too fast and is not conducive to exciton separation, resulting in low detector responsivity, which is limited to about 6.1 mA W^{-1} based on single-layer undoped graphene [41]. As a result, to overcome the above limitation, it is necessary to dope graphene with other materials. In addition, the graphene photodetector exhibits almost no attenuation in photoresponse in the modulation frequency range of 40 GHz, and the predicted theoretical bandwidth can be increased to 500 GHz, with a responsivity of 0.5 mA W^{-1} at 80 V bias. Using nanostructured plasmas to enhance the local optical fields and combining with waveguides to increase the length of the light–graphene interaction can improve the sensitivity of graphene photodetectors. Ding et al. fabricated waveguide-coupled integrated graphene plasmonic photodetectors on a Si platform with a bandwidth over 110 GHz and a high intrinsic responsivity of 360 mA W^{-1}, which was attributed to the plasmon-enhanced graphene–light interaction and subwavelength confinement of the optical energy [42]. Guo and co-workers proposed and realized high-performance waveguide photodetectors based on bolometric/photoconductive effects by introducing an ultrathin wide silicon−graphene hybrid plasmonic waveguide, which enabled efficient light absorption in graphene at 1.55 μm and beyond [43].

2.3.2. Organic Solar Cells

Organic solar cells have attracted increasing attention due to their light weight, easy fabrication, low cost, large-area processability, low in-plane resistivity, and excellent light transmittance [44]. Due to its excellent properties, graphene shows great application potential in organic solar cells and it is expected to be an ideal material to replace indium tin oxide [45]. Li et al. reported a highly efficient graphene–Si solar cell. the corresponding schematic illustration of this graphene–Si Schottky junction solar cell is shown in Figure 2 [46]. Liu et al. [47] prepared a package-free organic photovoltaic device using

highly doped multilayer CVD graphene as a top transparent electrode. The device with a double-layer graphene electrode exhibits the maximum power conversion efficiency of 3.2% and it has excellent bending stability. In addition, two or more layers of graphene top electrodes can well protect organic photovoltaic devices from air pollution because the multilayer graphene films are impermeable to air, which may simplify the device fabrication and decrease the cost of devices. Ricciardulli et al. [44] reported a cost-effective method for the fabrication of a transparent conductive electrode in an organic solar cell using solution-processed high-quality graphene. The obtained transparent electrode shows low sheet resistance and a high-power conversion efficiency value (4.23%) for an organic solar cell. In addition to graphene, graphene derivates such as graphene oxide (GO) also play an important role in enhancing the performance of organic solar cells. In organic electronics, poly(3,4-ethylenedioxythiophene): poly (styrene sulfonate) (PEDOT: PSS) is the most widely used hole transport or anode interfacial material. Although it has many merits such as high optical transparency and solution processability, it still meets some problems; for example, its high acidic and hygroscopic characteristics can damage the transparent electrode. In order to solve this problem, Hilal et al. fabricated GO/PEDOT:PSS as the hole transport layer of organic solar cells [48]. The device, based on GO/PEDOT:PSS, exhibits a maximum power conversion efficiency of 4.82%, and it retains over 30% of its initial power conversion efficiency without encapsulation after 15 days under atmospheric conditions. These excellent performances are attributed to the bond formation at the interface of the GO/PEDOT:PSS hole transport layer.

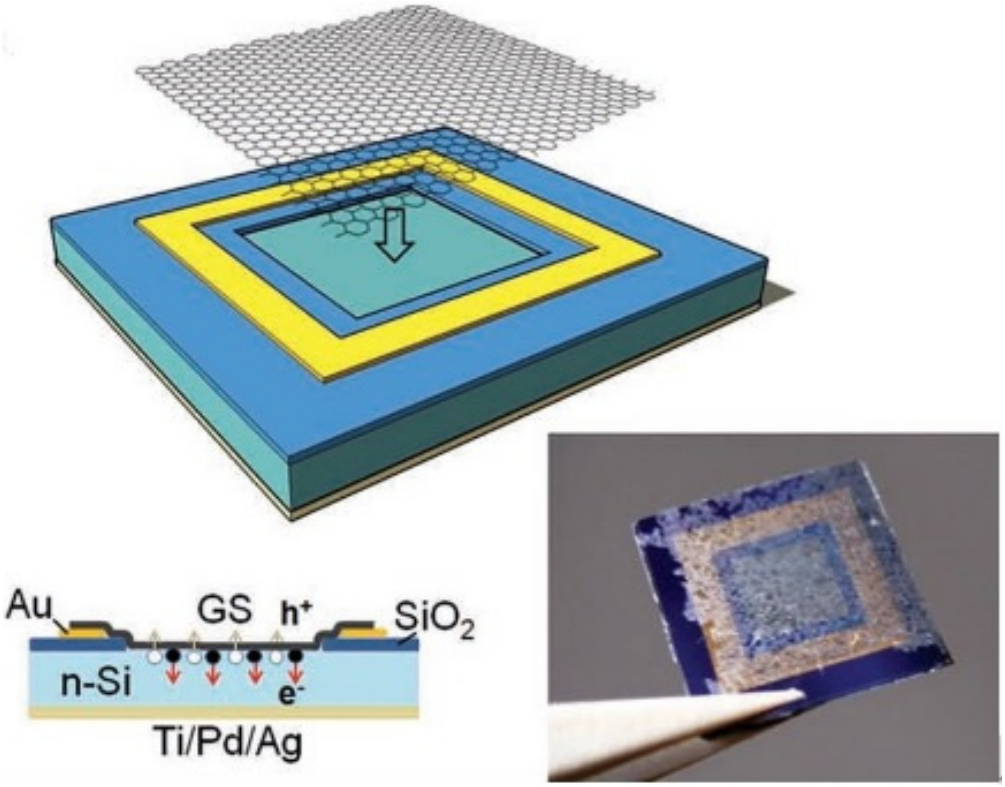

Figure 2. Schematic illustration of the device configuration. (Reproduced with permission from ref. [46]. Copyright 2010 Wiley Publications).

2.3.3. Graphene-Based Electromagnetic Optical Nanoantennas

Optical nanoantennas functioning at terahertz (THz) band, infrared and optical frequencies can control the energy conversion of light into localized energy and optical radiation at the subwavelength scale [27]. Therefore, they play an important role in the emerging field of photonics. The fundamental capabilities of nanoantennas can be utilized in practices including high-speed communication with high (gigabit/s) data rates in

nano-networks, inter-chip communication, THz detection, optical light emission, energy harvesting, and optoelectronic devices [49]. At the most progressive principle level, optical antenna devices can be separated into passive and active classes [50]. Passive devices are characteristically linear, for instance, plane optics and light emission, whereas active devices are nonlinear, converting optical light signals into electrical current and enhancing optical signals, i.e., photodetection and light energy harvesting [51].

Graphene doping with certain chemicals and by electric/magnetic biasing portrays a remarkable tenability [52]. Highly doped graphene has recently emerged as an appealing platform for plasmonics due to its unique optoelectronic properties, which give rise to relatively long-lived, highly confined, and actively tunable plasmon resonances that mainly appear in the infrared and THz frequency regimes [53,54]. The unique properties of graphene are exploited in nanoantennas such as reflectarray antennas [55], frequency reconfigurable antennas [56] and leaky-wave antennas [57,58], resonating at much lower frequencies compared with their metallic counterparts [59].

2.3.4. Optoelectronic Modulators

Graphene has strong inter-band optical transitions due to the strong interaction with light. It has an extremely wide spectral range under different conditions, strong nonlinearity and tunable Fermi energy levels, giving it many advantages in photoelectric modulators [60,61]. Researchers have made a graphene-based optical modulator with a broad optical bandwidth (1.35–1.6 mm); small device footprint (25 mm^2); and high operation speed (1.2 GHz at 3 dB) under ambient conditions, which is essential for optical interconnects for future integrated optoelectronic systems [9]. Christopher T. Phare et al. [62] reported a graphene electro-optic modulator that operates with a 30 GHz bandwidth and with a state-of-the-art modulation efficiency of 15 dB per 10 V. The graphene-based all-optical modulators (AOM) delivered the best performance among AOMs, presenting the smallest power threshold and fastest relaxation process [63]. Chi et al. fabricated a mid-infrared enhanced plasmonic modulator by integrating bilayer graphene in a reflective structure [64]. In comparison with monolayer graphene, bilayer graphene is highly doped to increase the carrier density in the modulator. The proposed modulator exhibits a modulation depth up to 21 dB and 3 dB with a bandwidth of 47.4 GHz over a wide range of wavelengths (3.17 μm to 4.4 μm). It can enable more efficient modulation with the same variation of Fermi levels than the modulator with monolayer graphene.

2.3.5. Graphene-Based Ultra-Fast Lasers

Graphene is an excellent wide-spectrum saturated absorber in the laser field because of its strong optical absorption capacity and fast carrier transport speed [65,66]. Lasers operating in the THz range can be used in a variety of applications because their beams can pass through many materials. However, these lasers have a fixed wavelength, greatly limiting their practical applications [67]. Graphene-based wavelengths can be changed in electric fields. Tunable graphene optical properties and GPs can be used to modulate the emission of a THz quantum cascade laser [68]. As illustrated in Figure 3, Marco Polini gained modulation by graphene plasmons in aperiodic lattice lasers using graphene to replace metal in a laser and placed them on the substrate in combination with aluminum gallium arsenide quantum dots and gallium arsenide wells with different thicknesses [69].

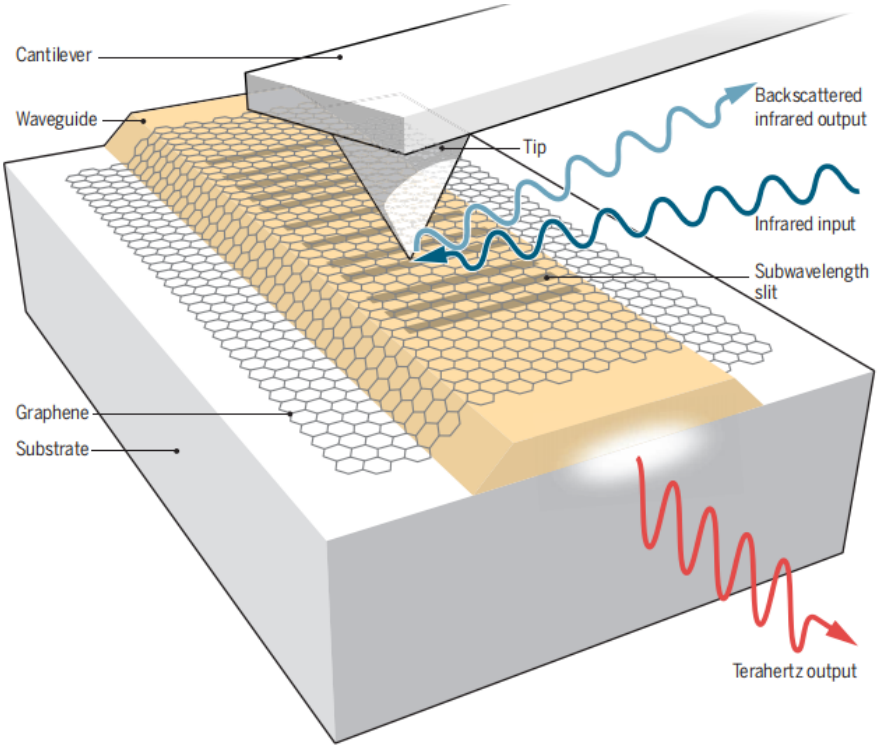

Figure 3. Probing plasmons in aperiodic lattice lasers. (Reproduced with permission from ref. [51]. Copyright 2016 American Association for the Advancement of Science Publications.).

3. Transition Metal Dichalcogenides

3.1. Basic Structure and Property

TMDCs are a class of materials with the formula of MX_2, where M is the transition metal element from group IV (Ti, Zr, Hf, and so on), group V (for instance V, Nb, and Ta) or group VI (Mo, W and so on), and X is a chalcogen (S, Se or Te) [70]. The structure of TMDC is shown in Figure 4a, and the chalcogen atoms are in two hexagonal planes which are separated by a plane of metal atoms [71]. Monolayer TMDC is typically 6–7 Å thick, depending on the material [72].

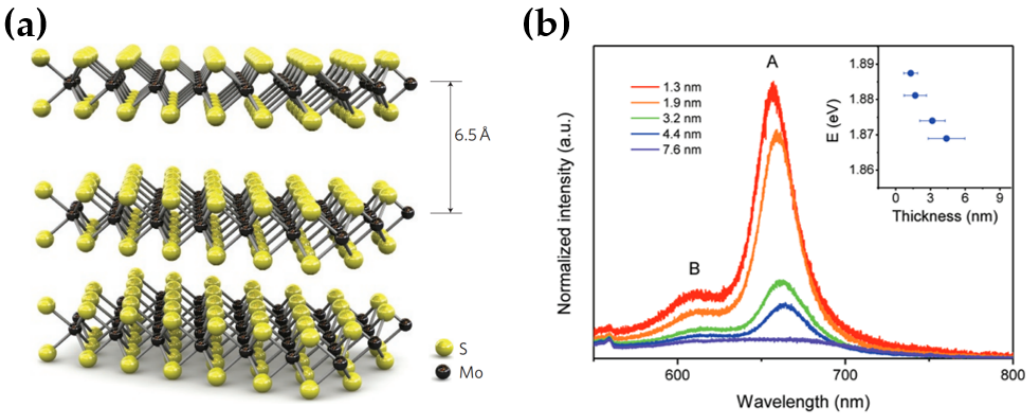

Figure 4. (**a**) Three-dimensional schematic representation of a typical MX_2 structure, with the chalcogen atoms (X) in yellow and the metal atoms (M) in grey [71] (Reproduced with permission from ref. [71]. Copyright 2016 Springer Publications.); (**b**) photoluminescence spectra of MoS_2 thin films with average thicknesses ranging from 1.3 to 7.6 nm (Reproduced with permission from ref. [73]. Copyright 2011 ACS Publications).

MX_2 are indirect bandgap semiconductors [74,75], whereas their monolayers have direct bandgaps, which are favorable for optoelectronic applications [76]. Native bandgap provides an excellent current on/off ratio in field-effect transistors (FETs) [77]. Their bandgap can be tuned based on the layer thickness, greatly expanding their range of applications in photonic devices.

TMDCs have excellent optical properties and a wide range of application prospects in the fields of light detection and photoluminescence. MoS_2 is a commonly used MX_2 nanomaterial. Although the photoluminescence of bulk MoS_2 is not obvious, the monolayer MoS_2 has strong photoluminescence [73], so the monolayer MoS_2 can be used in solar panels, photodetectors, and photovoltaic emitters.

The photoluminescence of TMDCs is closely related to the layer thickness. As shown in Figure 4b, the photoluminescence of MoS_2 increases as the number of layers decreases, and the strongest photoluminescence is observed for a single layer [73]. Photoluminescence and Raman characterizations show that the direct bandgap can be blue-shifted for ~300 meV per 1% strain, which can effectively modulate its energy band structure [78]. In addition, the doping treatment can also significantly modulate the photoluminescence peak intensity of MoS_2 [79].

3.2. Production Methods

The preparation of large-area, high-quality 2D TMDCs is a prerequisite for electronic device applications, and there are two main types of preparation methods: top-down and bottom-up methods [80]. The top-down method is a method to obtain 2D TMDCs by chemical or mechanical exfoliation from the bulk material, while the bottom-up method is a method to prepare 2D TMDCs by CVD or thermal decomposition. Exfoliation procedures can produce 2D materials with the best accessible quality, and thus the method is widely used to prepare samples for fundamental physics and device studies [81]. However, this method is time-consuming and cannot be scaled up, which will provide significant challenges for large-scale implementation in the future. Physical and chemical processes provide another way to manufacture nanosheet materials, with the intention of achieving controllable, high-quality, and large-scale nanosheets. Among the numerous chemical synthesis methods including CVD, the hydrothermal method, laser-induced synthesis, and molecular beam epitaxy (MBE), CVD has the most potential for realizing controllable, high-quality, wafer-scale 2D TMDCs; the flowchart is shown in Figure 5 [82]. PVD is also a viable option for producing high-quality TMDCs on a large scale. PVD has been proven on TMDCs films for several decades with homogeneity across wide areas for various materials, and it is created at low processing temperatures. The most often utilized PVD-based technologies investigated for depositing TMDCs materials include sputtering and pulsed laser deposition (PLD) [81,83,84]. PLD is an alternate method for synthesizing TMDCs thin films with a wide area and homogeneity at low growing temperatures. Except for Si substrate, PLD is also suitable for various substrates such as Al_2O_3, GaN, and SiC-6H [85], on which MoS_2 shows a high degree of crystallinity and out-of-plane texture. Anti-position defects are usually observed in the samples that are prepared via the PVD method, while the vacancy defects that are usually found in the TMDCs films are prepared by the CVD method [86]. PVD approaches can obtain large-scale and uniform TMDC films for devices and circuits. However, they perform at a lower quality than chemical methods and exfoliation approaches because of small domains and numerous defects [87].

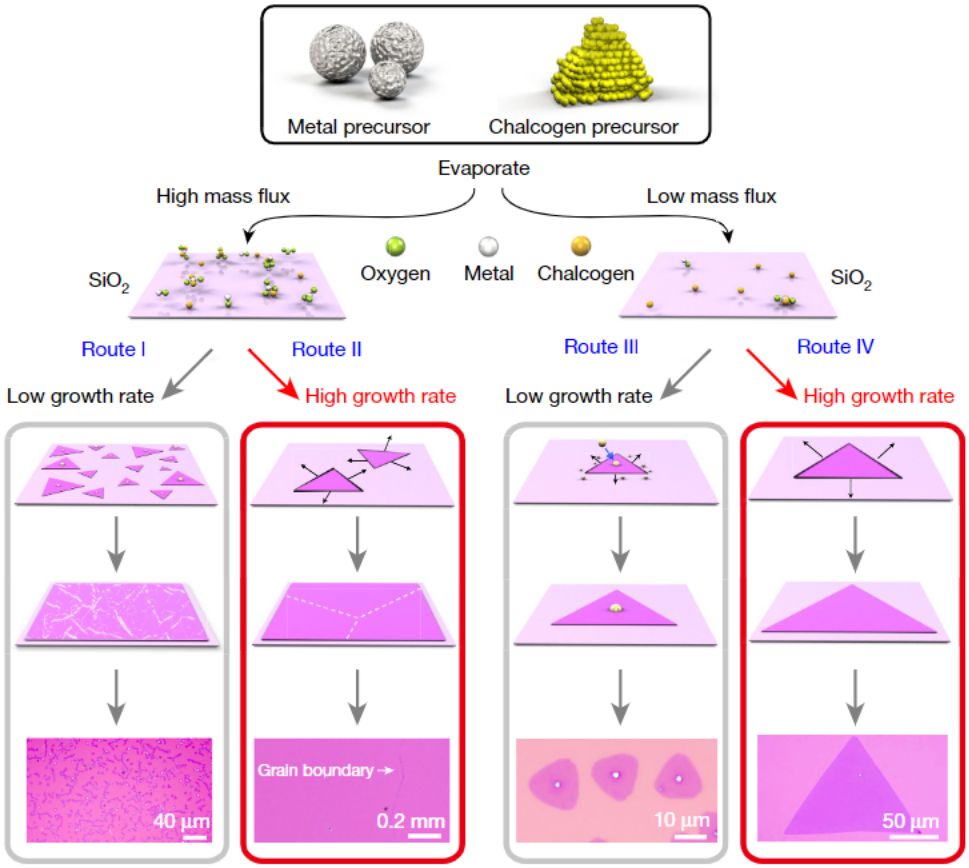

Figure 5. Flow chart of the general growth process for the production of TMDCs by the CVD method. (Reproduced with permission from ref. [82]. Copyright 2018 Nature Publications).

3.3. Optical Applications

Single-layer TMDCs are atomically thin and processable. They have primarily direct bandgaps; hence, they have great potential for applications in flexible and transparent optoelectronics.

3.3.1. Light-Emitting Diodes

A light-emitting diode (LED) is an optical source in which photons are generated by the electroluminescence (EL) effect [88,89]. Electrons and holes are permitted to recombine in a p-n junction so that the recombination energy can be released as photons in response to injected electrical bias currents. This is because of the availability of a large variety of direct bandgap TMDC monolayers with excellent photoluminescence quantum yield at sub-nanometer thicknesses [90–92]. TMDC materials have recently been investigated for their usage in LED fabrication. Due to several thermally aided processes resulting from impact ionization across a Schottky junction or a p-n junction [93–95], the EL is observed in various MoS_2 monolayer based devices [95]. However, because of the low optical quality of MoS_2 and the inadequate electrode connections, poor EL efficiency and considerable linewidth widening are found [96]. Due to the decreased contact resistance, increased current density, and the effective current injection, 2D TMDC-based heterostructure LEDs exhibit a high EL efficiency [96]. Electrically adjustable excitonic LEDs with p-n junctions based on WSe_2 monolayers may effectively inject electrons and holes; the corresponding structure is shown in Figure 6.

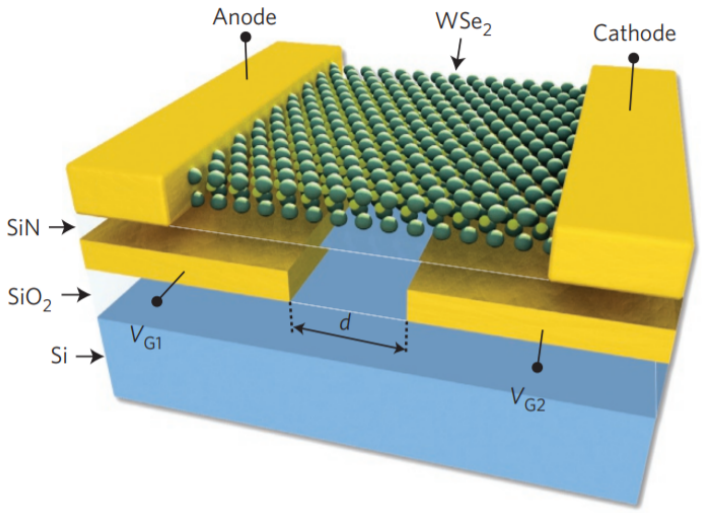

Figure 6. WSe_2 monolayer device with split gate electrodes (Reproduced with permission from ref. [95]. Copyright 2014 Springer Nature Publications).

3.3.2. Solar Cells

As clean and renewable energy sources are widely studied, the photovoltaics (PV) effect has attracted the attention of many because it shows great application potential in energy harvesting. Due to the enormous surface area, lack of dangling chemical bonds on surfaces, and their potential as sunlight absorbers, 2D TMDC materials are regarded as promising prospects for solar applications. Two-dimensional TMDCs are applied in solar cells by forming a Schottky or p-n junction that works as an interface for the separation of charge carriers. TMDCs (MoS_2, $MoSe_2$, and WS_2) can absorb up to 5–10% incident sunlight in a monolayer (thickness less than 1 nm). The absorption of sunlight is one order of magnitude more than that of typical semiconductors such as GaAs and Si. The efficiency of solar cells based on ultrathin TMDCs is limited by the loss of absorption under the thickness limitation [97]. Calculations suggest that a monolayer TMDC could absorb as much sunlight as 50 nm of Si and generate electrical currents as high as 4.5 mA cm^{-2} [98]. There are three ways to improve the performances of TMDC solar devices [99]: (1) careful control over the doping levels of TMDCs and Si, which would reduce the series resistance of the device; (2) utilization of large-area grown or deposited materials; (3) incorporating additional 2D semiconducting layers such as WSe_2 with complementary absorption spectra. In recent years, ultrathin solar cells have drawn much attention due to the possible reduction in cost and semiconductor material consumption, as well as their suitability for flexible and ultralight photovoltaics. A 120 nm thick MoS_2 p-n junction is presented [100]. Researchers have developed a straightforward method to fabricate ohmic contacts to both n and p MoS_2 and added an h-BN layer on top of the semiconductor to minimize the reflectance of the front surface. The homojunction device exhibits (3.8 ± 0.2)% efficiency and a 57% fill factor under AM1.5G illumination, which contributes to the maturity of the emerging technology of TMDC-based ultrathin solar cells. The incorporation of WS_2 as a photovoltaic material was presented [101]. With this optimized deposition parameter, WS_2 thin film was successfully fabricated for the very first time as a window layer in CdTe solar cells. The new device (ITO/WS_2/CdTe/CuC/Ag) exhibited V_{oc} = 0.39 V, J_{sc} = 10.45 mA cm^{-2}, fill factor = 29.42%, and efficiency = 1.2%. Shin et al. fabricated an organic solar cell (TFSA-GR/MoS_2/P3HT:PCBM/Al) by using MoS_2 as a hole transport layer, bis(trifluoromethanesulfonyl)-amide-doped graphene (TFSA-GR) as a transparent conductive electrode, and a GR quantum dots (GQDs)-added active layer [102]. They investigated the effect of the number of layers (L_n) of MoS_2 on the power conversion efficiency of organic solar cells. When L_n = 2, the fabricated solar cell shows a maximum power conversion efficiency of 4.23%. When L_n = 1, the power conversion efficiency is small because of the low absorption in the visible region. While L_n > 2, the power conversion

efficiency is also lowered due to the lower amount of sunlight reaching the active layer. As a result, the selection of a suitable L_n of MoS_2 plays an important role in the performance of solar cells.

3.3.3. Photodetectors

Photodetectors have been the most extensively researched optoelectronic device for TMDCs, with research ranging from novel device topologies to utilizing unique physical features to strategies to improve performance [103–106]. A 3D schematic of supported and suspended channel FET architectures with ReS_2 as the channel material is shown in Figure 7 [107]. ReS_2 has been shown to have an anisotropic band structure resulting in two major excitons with unequal binding energy [108–110]. This allows control over polarized light absorption, and the consecutive polarization of a sensitive photodetector. The appropriate calibration of such photodetectors permits the detection of both light intensity and polarization, allowing for the detection of polarization-encoded messages. Some reports on photodetectors consisting of TMDC materials are listed in Table 2.

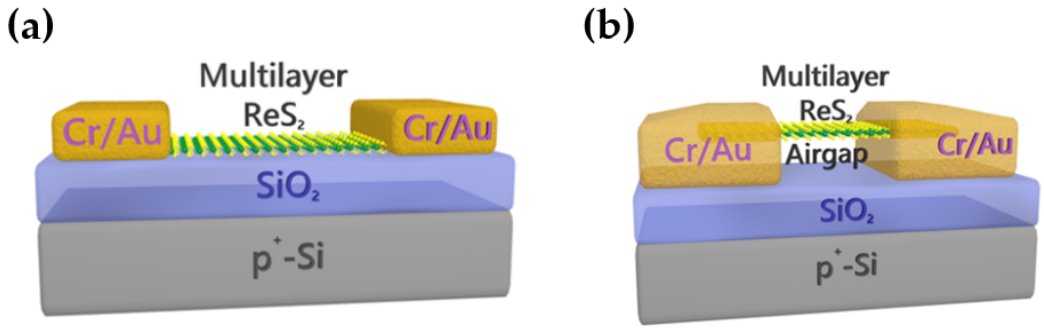

Figure 7. (**a**) Schematic of supported (in contact with back-gate dielectric) channel ReS_2 transistors under 633 nm focused laser excitation; (**b**) schematic of suspended (airgap between channel and back-gate dielectric) channel ReS_2 transistors under 633 nm focused laser excitation (Reproduced with permission from ref. [107]. Copyright 2018 ACS Publications.).

Table 2. Photodetectors based on TMDC materials.

Material	Laser λ (nm)	Intensity (mW cm^{-2})	Detectivity (Jones)	Response Time (s)	Responsivity (A W^{-1})	Ref.
MoS_2	635	0.1	7.7×10^{11}	8.0×10^{-3}	5×10^4	[111]
ReS_2	532	-	1.2×10^{12}	100	8.86×10^4	[112]
ReS_2	589	0.12	-	3.2	654	[113]
$MoTe_2$	1064	-	-	2.4×10^{-5}	0.11	[114]
WSe_2/ZnS_2	520	100	4.7×10^{10}	5.0×10^{-4}	0.1087	[115]
ReS_2	630	140	-	2.0×10^{-6}	4	[107]
WSe_2/ZnS_2	550	3.77	1.3×10^{13}	0.25	11.5	[116]
WS_2	1310	-	3.0×10^{11}	3.2×10^{-2}	510	[117]
MoS_2	1310	-	1.0×10^{11}	0.2	103	[117]
MoS_2-ZnCdSe	450	-	1.0×10^{12}	1.2	3.7×10^{-4}	[118]
MoS_2	532	1	1.0×10^{12}	0.5	150	[119]
MoS_2	442	0.6	5.0×10^{11}	-	186	[120]
$AgBiBr_6/WS_2$	455	0.071	1.5×10^{13}	5.23×10^{-5}	0.52	[121]

Mixed dimensional heterostructures and plasmonic-, organic material- or quantum dot-enhanced structures have been studied for performance enhancement [113,122,123]. According to preliminary research, photodetectors based on MoS_2 monolayers have better photoresponsivity than graphene-based devices [124,125]. $MoS_2/SnSe_2$ heterostructure-based photodetectors exhibit a high responsivity of up to 9.1×10^3 A W^{-1}, which is significantly greater than MoS_2 only film-based photodetectors [126]. The photoexcited electron-hole pairs of GaTe-MoS_2 p-n heterojunction phototransistors are separated by large

built-in potential, formed at the GaTe-MoS_2 interface efficiently to generate a self-driven photocurrent within <10 ms [127]. Two-dimensional TMDCs heterostructures can also be explored for possible THz detection at room temperature [128].

4. Other 2D Materials

4.1. Black Phosphorus

4.1.1. Morphology and Structure

Black phosphorus (BP) is a stable layered structure similar to 2D structures such as graphene and TMDCs [129]. Like bulk graphite, BP has a layered substance in which individual atomic layers are stacked together by van der Waals interactions and can be similarly isolated from black phosphorus by the mechanical exfoliation method. BP is not planer but puckered due to the sp^3 hybridization. Each phosphorus atom is covalently bound with three adjacent phosphorus atoms inside a single layer to form a puckered honeycomb structure (Figure 8) [130].

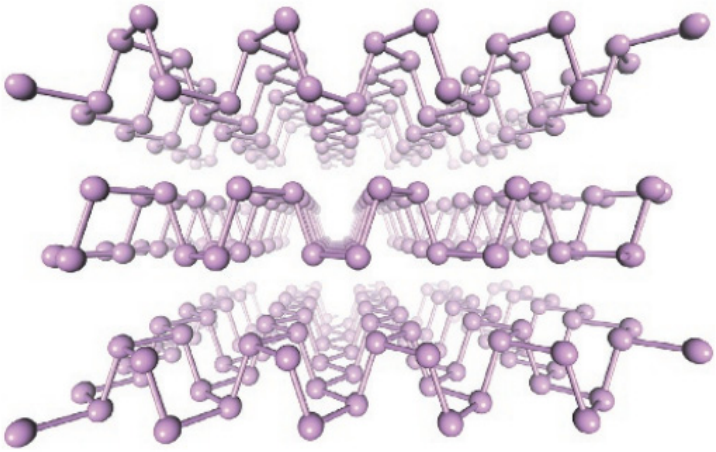

Figure 8. Atomic structure of BP. (Reproduced with permission from ref. [131]. Copyright 2014 Springer Nature Publications).

4.1.2. Optical Properties

The direct bandgap (≈0.3 eV) of BP thin film (eight layers, or thickness > 4 nm) can link the energy gap between the zero bandgap of graphene and the comparatively large bandgaps of numerous TMDCs (1.5–2.5 eV) [16,132–134]. Unlike graphene and TMDCs, the bandgap of few-layer BP can be tuned by interlayer interactions and is strongly dependent on the number of layers.

Due to the "puckered" crystal lattice, BP shows strong band dispersion anisotropy [135]. The anisotropic absorption was identified with a maximum absorption value of 28% in the mid-infrared region when the incident light was polarized along the armchair direction of BP [136]. Thin-film BP has also been widely applied for mid-infrared ultrafast photonics as saturable absorbers due to the decent optical absorption. BP exhibits broadband absorption from the visible to the mid-infrared spectral region, which is also manifested by the broadband nonlinear optical response. Multilayer BP flakes of 3–20 nm thickness dispersed in liquid exhibit strong saturable absorption at both 400 nm and 800 nm, as measured by the z-scan technique and shown in Figure 9a,b [137]. In multilayer BP, one photon provides sufficient energy to excite an electron from the valence band to the conduction band under femtosecond laser excitation of 400 nm (3.1 eV) and 800 nm (1.55 eV) wavelengths, whereas in monolayer BP, two photons must arrive simultaneously, as shown in the inset of Figure 9c [137].

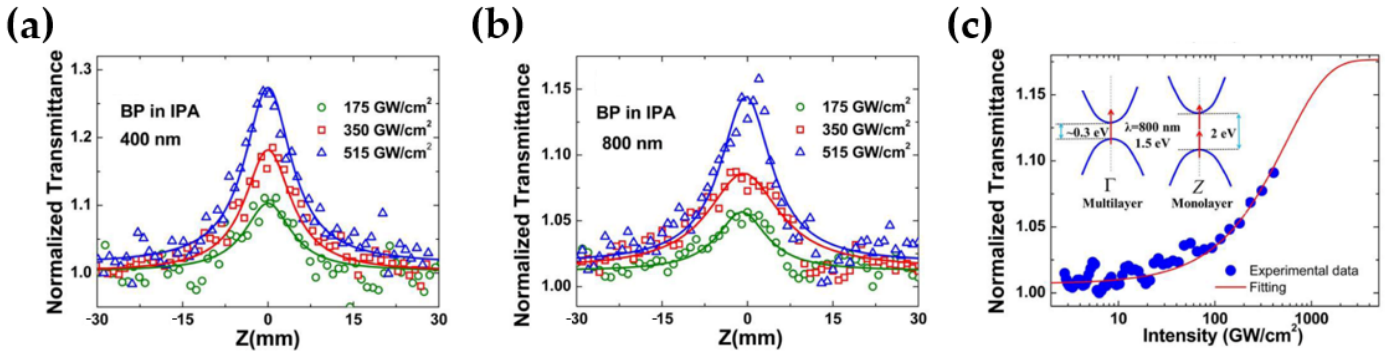

Figure 9. Broadband nonlinear optical absorption of BP dispersions. The open-aperture Z-scan measurements of dispersions of BP nanoplatelets under different intensities at 400 (**a**) and 800 nm (**b**), respectively; (**c**) relation between normalized transmittance and input intensity for dispersions of BP NPs at 800 nm. (Reproduced with permission from ref. [137]. Copyright 2015 OSA Publications).

The robust optical conductivity of BP thin film in the wavelength range from 1 to 5 μm suggests BP as an attractive contender for near- and mid-infrared optoelectronics applications such as modulators, photodetectors, ultrafast optical switches, and, possibly, light-generation devices such as LEDs and ultrashort pulsed lasers [138].

4.1.3. Optical Applications

Numerous studies have also been performed on the applications of BP in photodetectors [139–141], polarization-sensitive detectors [142,143], saturable absorbers [144,145] and emitters [146], and photovoltaics devices [147,148].

Because of the direct bandgap and high carrier mobility, BP is promising in building broadband phototransistors for imaging and photodetection, especially in the near-infrared and mid-infrared wavelengths [149]. The response wavelength range of BP-based photodetectors can be increased by an external vertical electric field because the optical bandgap of few-layer BP is highly adjustable by the quantum-confined Stark effect [150–152]. Different portions of a single BP flake can be adjusted into opposing doping regimes to create an artificial PN junction that can generate a photocurrent via the photovoltaic effect. Because of the versatility and compatibility of 2D BP, it can be combined with other nanomaterials to improve the performances of photodetectors [153–155]. BP can be combined with other low-dimensional nanomaterials such as nanowires and quantum dot [156,157], allowing for the creation of unique heterostructures based on materials with different/multiple dimensions. BP is also an excellent midinfrared electro-optic material for modulation applications due to its solid electro-optical response and relatively small bandgap.

4.2. 2D Transition Metal Carbides MXenes

Transition metal carbides, carbonitrides, and nitrides were first discovered and termed MXenes (MX) by Barsoum et al. in 2011 [158]. The common formulation of MXs is $M_{n+1}X_nT_x$, where M embodies the transition metals (such as Ti, Ta, Mo, and Cr); X signifies nitrogen or carbon, n may differ from 1 to 4; and T_x denotes surface ends on the outer M layers (such as -O, -OH, -F, and -Cl) [159]. M^1 and M^2 are two different Ms. In case two different Ms have in-plane arranging and form rotating chains of M^1 and M^2 molecules inside the similar M layer, the ensuing MX configuration is known as i-MX with a general formula of $(M^1_{4/3}M^2_{2/3})XT_x$, where the percentage of every compound is mentioned as a decimal value. The M^1 and M^2 molecules positioned in distinct atomic planes holding an out-of-plane arrangement are known as o-MXs, in which M^2 molecules compose the internal layers and M^1 molecules are in the exterior surface. o-MXs are represented by two chemical formulations as $(M^1_2M^2)X_2T_xTx$ and $(M^1_2M^2_2)X_3T_x$. MXs with V, Ti, Nb, Cr, Mo, Zr, Sc, Hf, Ta, Y, and W in the M spot were investigated. W, Sc, Y, and Cr have only

been registered as elements of i-MXs, o-MXs, or in combination with the other metals listed above [160].

4.2.1. Morphology and Structure

MXenes consist of a transition metal-made (M) hexagonal close-packed crystal symmetry, and the X molecules occupy an octahedral spot between the adjacent M layers [159]. MXenes can be classified as ordered mono-M, ordered double-M and solid-solution M elements based on their atomic lattices and composition, as shown in Figure 10 [161].

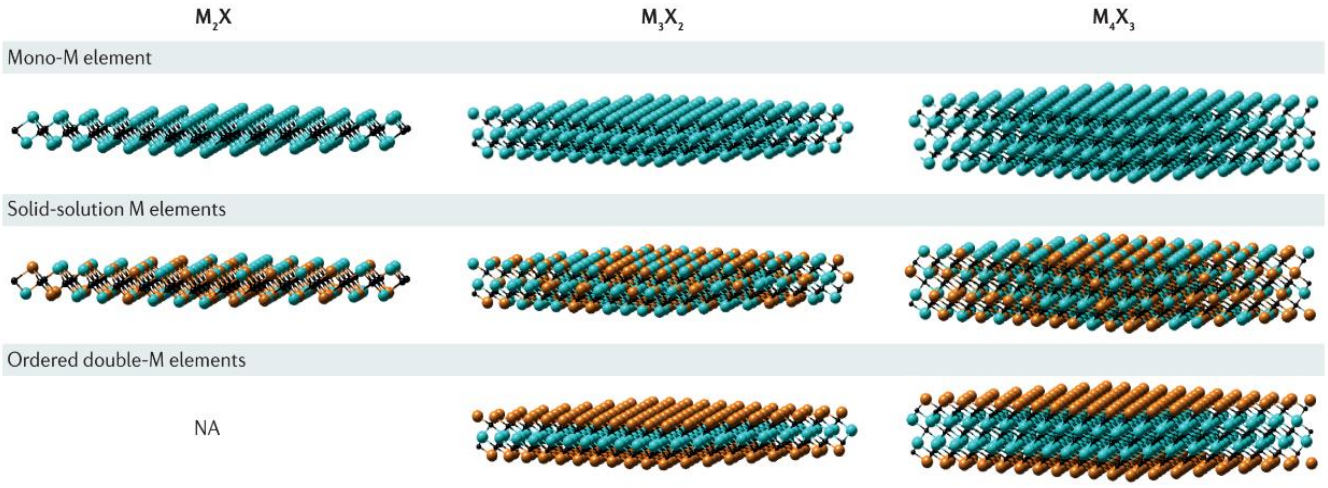

Figure 10. Typical layered structures of MXenes. (Reproduced with permission from ref. [161]. Copyright 2017 Springer Nature Publications.).

4.2.2. Optical Properties

MXenes have unique optical properties and a wide range of tunability, making them ideal materials for a variety of optical applications. Because of their large density of states at the Fermi level, MXenes have intriguing transport features, while TMDCs have low carrier mobility. MXene films have been found to exhibit a broadband optical transmittance of more than 90% [162,163], with a transmission valley of around 750–800 nm [164], which has been attributed to the surface plasmon resonance (around 780 nm) and inherent out-plane interband transitions (around 800 nm). When compared with the pristine MXene, the oxidized sample has a higher absorption in the visible region, while fluorinated and hydroxylated MXenes have a lower absorption. In the ultraviolet optical region, all functional groups lead to an enhancement of both the absorption and reflectivity of MXenes [165]. $M_{n+1}X_n$ with a smaller n is expected to be more transparent than MXenes with a larger n due to the lower density of states [165,166].

Both MXenes quantum dots and nanosheets exhibit strong photoluminescence due to the direct bandgap, which allows for radiative electronic transitions [167,168]. MXene quantum dots typically have three absorption peaks at 260 nm, 310 nm, and 350 nm, depending on the particle size and composition. The excitation wavelengths have a big impact on the photoluminescence spectral band. For example, as shown in Figure 11, the photoluminescence spectra of Ti_3C_2 quantum dots range from 400 to 600 nm when the excitation wavelengths vary from 340 to 440 nm [167].

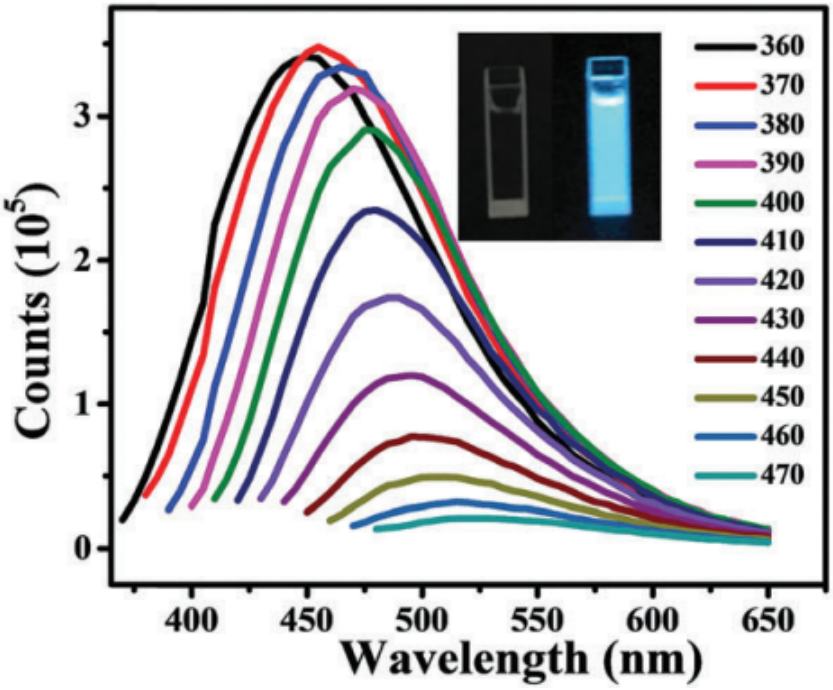

Figure 11. The photoluminescence spectra of Ti_3C_2 quantum dots under different excitation wavelength. (Reproduced with permission from ref. [167]. Copyright 2018 RSC Publications.).

4.2.3. Optical Applications

The MXenes such as $Ti_3C_2T_x$ slim layers are well-suited for optoelectronic applications which require adaptive translucent conductive electrodes due to their high transparency and low layer resistance [169]. Translucent conductive electrodes based on MXenes have been used to provide appropriate volumetric capacitance in translucent solid-state supercapacitors [162]. Except translucent conductive electrodes, MXenes also show great potential applications in other optical applications. For example, $Ti_3C_2T_x$ nanostructures have been widely used to realize ultrafast pulses in different lasers. In 2017, Jhon et al. reported MXene-based SA-activated ultrafast pulses, which achieved mode-locking at 1.5 m-band and q-switching pulses at 2 m-band, respectively [170]. MXenes exhibit excellent broadband saturable absorption capability in the near-mid-infrared region [171]. In 2019, Yi et al. reported the broadband nonlinear properties of MXenes in the three-wavelength band, in which mode-locked pulses operating at 1051 and 1565 nm and q-switched pulses operating at 2798 nm were realized using the same Ti_2CT_x-based SA [172]. A total of 1.2 nm of spin-coated Ti_3C_2T MXene film on glass, quartz and polyetherimide substrates achieves an ultra-low optical attenuation of 3% in the visible region [173]. It is noteworthy that the prepared Ti_3C_2T MXene films have a transmittance of up to 98% and can be used for flexible and conductive high-capacity capacitors [162,174]. In addition, $Ti_3C_2T_x$ nanosheets can be easily oxidized to TiO_2 during the delamination process. If stored in an oxygen-rich atmosphere, $Ti_3C_2T_x$-TiO_2 nanocomposites can be obtained in situ, further expanding their applications in electrochemical and optoelectronic devices. In 2008, Mochalin et al. prepared $Ti_3C_2T_x$-TiO_2 nanocomposites by the in situ oxidization of $Ti_3C_2T_x$ for UV photodetection [175]. $Ti_3C_2T_x$ MXenes can also serve as electron and hole collection layers in solar cells [176], accelerating charge extraction and improving photovoltaic efficiency. Meanwhile, doping $Ti_3C_2T_x$ MXenes into the electron transport layer, hole transport layer or activation layer can change the energy level and improve the electrical conductivity and carrier mobility. For example, Agresti et al. used $Ti_3C_2T_x$ with different termination groups (T_x) to tune the work function of the perovskite absorber and the TiO_2 electron transport layer, as well as to engineer the perovskite/electron transport layer interface [177]. The combined effect of work function tuning and interface engineering can significantly

improve the performance of MXene-modified perovskite solar cells. Compared with the reference cell without MXene, the power conversion efficiency was improved by 26% and the hysteresis was reduced.

4.3. Hexagonal Boron Nitride

4.3.1. Morphology and Structure

hBN is one of the key 2D materials composed of alternating B and N atoms bonded by sp^2 covalent bonds in its hexagonal lattices. hBN crystal contains alternating B and N atoms in a base plane and, thus, has great variations in growth kinetics due to its different edge terminations. As a result, the morphologies of h-BN domains are varied with its B or N terminations (Figure 12) [178].

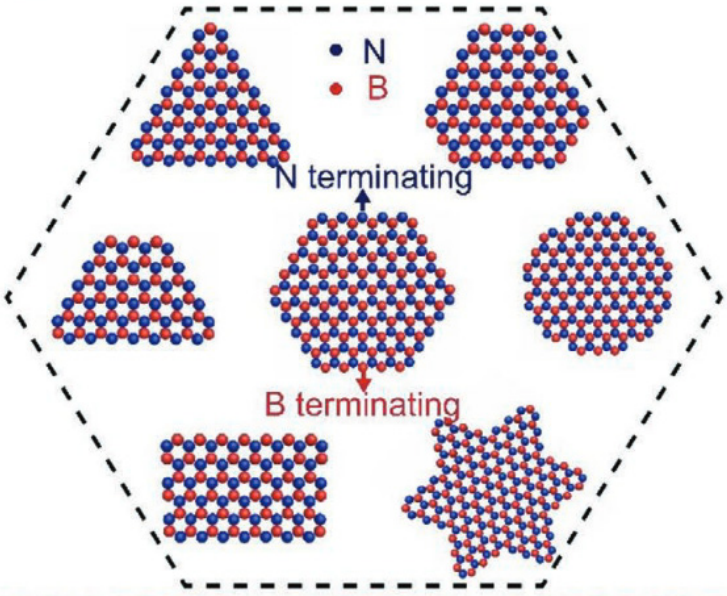

Figure 12. Different shapes of h-BN domains with B or N atoms terminating (Reproduced with permission from ref. [178]; Copyright 2018 RSC Publications.).

4.3.2. Optical Properties

Despite the fact that hBN is an indirect bandgap semiconductor (with an energy gap of about 6 eV) [179], it has a very high internal quantum efficiency for deep UV emission (up to 40%). The frequency of the normal lattice vibrational modes (optic phonons) is similarly very anisotropic due to the highly anisotropic crystal structure of hBN, with two different optic phonon branches. When monolayer hBN was placed on different substrates and under THz irradiation, the carrier density could be enhanced considerably, especially on SiO_2/Si substrate, which suggested that the SiO_2/Si substrate was more appropriate for the construction of monolayer hBN-based electronic and optoelectronic devices when compared with quartz, PET, and sapphire [180]. The wavelength responses of S-doped hBN monolayer films on molten Au substrates are extended to 280 nm, and the photocurrent and responsivity for light irradiation with a wavelength of 280 nm are ~50 times higher than that of pristine hBN, as shown in Figure 13a,b [181].

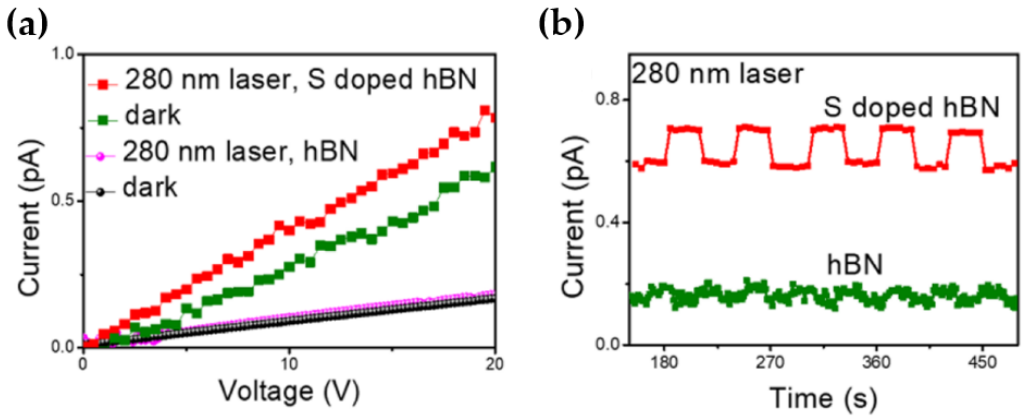

Figure 13. (**a**) I−V curves of hBN and S-doped hBN measured in the dark and 280 nm light irradiation at 20 V; (**b**) I−t curves of hBN and S-doped hBN under 280 nm light irradiation. (Reproduced with permission from ref. [181]; Copyright 2022 ACS Publications).

4.3.3. Optical Applications

h-BN shows great potential applications in many optical areas and some applications are summarized in Table 3. h-BN can be used as a wide bandgap semiconductor for deep-UV emitters and detectors because of its large bandgap. To further improve the response rate and detection rate, it is necessary to modulate the optical and electrical properties of hBN. Tan et al. successfully prepared S-doped hBN monolayers on molten Au substrates by atmospheric CVD, and they systematically studied their optical and electrical properties [181]. The band gap is reduced from 5.83 eV to 5.69 eV, and the conductivity is reduced by 140 meV. Moreover, the response range of the photodetector is extended to a 280-nm wavelength; the power density of the light source is 16.1 μW mm^{-2} (280 nm); and the responsiveness of the device with single, double and three-layer hBN is 3.63, 3.54 and 0.24 A W^{-1}, respectively. In addition, numerous studies have shown that hBN is also an excellent insulator that can be used as a substrate material for graphene-based devices [182,183]. Wu et al. demonstrated a deep ultraviolet photodetector based on a graphene/hBN/n-AlGaN heterostructure. The device not only exhibits high responsivity under UV illumination, but also exhibits a high UV/Vis rejection ratio. Several nanolayered graphene-hBN heterostructures are used to enhance the performance of photodetectors, successfully solving the strain problem between graphene and traditional bulk insulators [25]. Two-dimensional hBN film can provide almost ideal passivation due to its wide bandgap, no dangling bond and high dielectric constant. Raj et al. reported the passivation properties of monolayer hBN that was grown by metal-organic CVD [184]. Using an ITO/I-INP/P-INP solar cell structure with a small amount of hBN monolayer as the passivation layer, the solar cell performance is significantly improved. The maximum efficiency of five-monolayer (ML) hBN is 17.2%, V_{oc} is 0.78 V, J_{sc} is 29.4 mA cm^{-2}, and FF is 75.2%. The INP solar cell with 7 ML hBN has a measured efficiency of 15.7%, V_{oc}, J_{sc} and FF are 0.8 V, 27.1 mA cm^{-2} and 72.1%, respectively [184].

Table 3. Optoelectronic devices based on hBN.

Applications	Materials	Intensity	Detectivity (Jones)	Response Time	Responsivity	Ref.
Photodetectors	hBN/Cu	9.937 $\mu W\ cm^{-2}$	6.1×10^{12}	0.2 s	5.022 A W^{-1}	[185]
	graphene/hBN/n-AlGaN	16.1 $\mu W\ mm^{-2}$	1.76×10^{12} (monolayer hBN)	1.42 s	3.63 A W^{-1} (280 nm)	[186]
			2.05×10^{12} (bilayer hBN)	1.14 s	3.54 A W^{-1}	
			9.88×10^{10} (trilayer hBN)	1.13 s	0.24 A W^{-1}	
	hBN/black arsenic phosphorus/hBN				190 mA W^{-1} (3.4 μm) 16 mA W^{-1} (5.0 μm) 1.2 mA W^{-1} (7.7 μm)	[187]
	S-doped h-BN on Au substrate	0.2 $\mu W\ mm^{-2}$			~0.018 mA W^{-1} (280 nm) ~1 mA W^{-1} (230 nm)	[181]
	Materials	**Power conversion efficiency**	**V_{oc}**	**J_{sc}**	**FF**	
Solar cells	ITO/I-INP/P-INP/5 ML hBN	17.2%	0.78 V	29.4 mA cm^{-2}	75.2%	[184]
	ITO/I-INP/P-INP/7 ML hBN	15.7%	0.80 V	27.1 mA cm^{-2}	72.1%	
	MoS_2/WSe_2/h-BN surface passivation layer	Enhance 74%	0.38 V	1.69 mA cm^{-2}	-	[188]

4.4. 2D Metal Oxide

4.4.1. Basic Structure and Optical Properties

Two-dimensional metal oxides, formed by the O element and the metallic element, are gradually attracting more attention [189,190]. This is because they are not only rich in material species, but also contain a variety of structures including a nonlayered structure, a layered structure such as MoS_2, and inorganic molecular crystal. The special structure of 2D metal oxides endow these materials with numerous outstanding properties. Compared with typical 2D materials such as graphene and BP, 2D metal oxides possess many special characteristics. For example, they have excellent air stability due to the involvement of O and the relatively stable valence state of the elements that are contained in 2D metal oxides [191]. Second, 2D metal oxides generally have low requirements for a synthetic environment. Some 2D metal materials can even be obtained in an atmospheric environment. Third, most reported 2D metal oxides have wide bandgaps and exhibit excellent ultraviolet detection performances. As a result, they show great application potential in optoelectronics.

4.4.2. Optical Applications

Due to the unique performances of 2D metal oxides, they have been widely used in the fabrication of photodetectors, and some applications are summarized in Table 4. Recently, Yu et al. fabricated a photodetector based on ZnO nanosheets [192]. At a visible-blind wavelength of 254 nm, this photodetector exhibits a high responsivity up to 2.0×10^4 A W^{-1} and high detectivity (6.83×10^{14} Jones). Messalea et al. reported an ultra violet photodetector

based on ultrathin bismuth oxide (Bi_2O_3) nanosheets that were synthesized by a liquid metal facilitated approach [193]. The photodetector shows a high responsivity of about 400 A W^{-1} and a fast response time of ~70 µs at the wavelength of 365 nm. In addition to the application of photodetection in ultraviolet, 2D metal oxides can also be used in the long-wave-length infrared (LWIR) detecting devices. Yin et al. synthesized air-stable nonlayered ultrathin Fe_3O_4 nanosheets by a space-confined CVD approach [194]. The prepared Fe_3O_4 nanosheets can be used to fabricate high-performance ultrabroadband photodetectors with a detection range from ultraviolet to LWIR. Due to the synergistic mechanisms of the photoconductive effect and bolometric effect, the photodetectors exhibit an ultrahigh photoresponsivity of 562.1 A W^{-1}, a detectivity of 7.42 × 10^8 Jones, and an external quantum efficiency of 6.6 × 10^3% at the laser wavelength of 10.6 µm. Some 2D materials have a low symmetric crystal structure, leading to in-plane optical anisotropy [191]. Zhong et al. synthesized large-size 2D α-MoO_3 single crystals with structural in-plane anisotropy, which showed a remarkable ultraviolet photoresponse and electron transport anisotropies [195]. The photodetectors based on α-MoO_3 demonstrate a photoresponsivity of 67.9 A W^{-1} and an external quantum efficiency of 3.3 × 10^4% under solar-blind ultraviolet light (254 nm). Importantly, the photodetectors exhibit strong in-plane anisotropy in the optoelectronic response and transport properties. Although some photodetectors based on 2D metal oxides show excellent performances, there is still a long way to go for them to achieve practical applications. Exploring methods to produce high-quality 2D metal oxides is one of the effective ways to drive the further development of high-performance photodetectors. We believe that with the deepening of research, more and more photodetectors with outstanding performances will be fabricated.

Table 4. Photodetectors based on 2D metal oxides.

Materials	Wavelength	Responsivity	Detectivity	Ref.
ZnO	254 nm	2.0 × 10^4 A W^{-1}	6.83 × 10^{14} Jones	[192]
Fe_3O_4	10,600 nm	562.1 A W^{-1}	7.42 × 10^8 Jones	[194]
Bi_2O_3	365 nm	400 A W^{-1}	1.1 × 10^{13} Jones	[193]
α-MoO_3	254 nm	67.9 A W^{-1}	-	[195]
B-Ga_2O_3	254 nm	335 A W^{-1}	-	[196]
MgO	150 nm	1.86 A W^{-1}	1.8 × 10^{10} Jones	[197]

5. 2D Heterojunction Materials

5.1. Morphology and Structure

Atomically thin 2D materials with a wide range of properties can be manufactured and engineered separately and then stacked together to form van der Waals heterostructures (such as graphene-hBN, graphene-BP, TMD-hBN, graphene-TMDs, and TMD–TMD) [198], resulting in surprising novel optical properties for functional devices [199]. Different atomically thin 2D materials can be simply vertically stacked together to produce 2D heterostructures, which not only avoids the traditional issue of lattice mismatch, but can also introduce many outstanding physical or optical properties. The most widely utilized 2D material in heterostructures is hBN, primarily owing to its role as the 'ideal substrate' for graphene [200,201].

5.2. Optical Properties

Three types of heterojunctions (types I, II, and III) can be easily built by employing chosen materials based on various combinations of band alignments, depending on the energy difference between the conduction and valence-band extrema in the constituent layers (Figure 14) [202]. The valence band maximum and conduction band minimum of two separate components are positioned on the same side of the heterointerface in type-I (straddling gap) heterojunctions, and radiative recombination is enhanced as both electrons and holes reside in one material. Type-I heterojunctions have a quantum well structure, which makes them suitable for optoelectronic devices such as LEDs. The conduction

band minimum and valence band maximum in type-II (staggered gap) heterojunctions belong to two independent components with different work functions, providing chances to regulate the interlayer transition energy and to generate charge spatial separation. When the valence band maximum of one semiconductor is higher than the conduction band minimum of the other semiconductor, it consists of type-III (broken gap) heterojunction, and this unique electronic structure is very useful for tunnelling devices such as negative differential resistance devices.

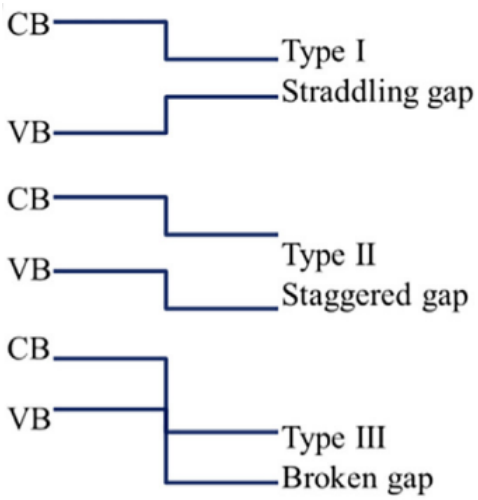

Figure 14. Schematic energy band diagrams of the three types of semiconductor heterojunctions: type-I (straddling gap); type-II (staggered gap); and type-III (broken gap) heterojunctions. (Reproduced with permission from ref. [202]. Copyright 2019 Elsevier Publications.).

The $MoSe_2$/BP and WSe_2/BP vdW heterostructures possess a direct bandgap, which is characterized by type-II band alignment, and demonstrate powerful built-in electric field across the interface, which can effectively separate the photogenerated charges. Figure 15 shows the light absorption capacity of MoS_2/BP, $MoSe_2$/BP, WS_2/BP, and WSe_2/BP vdW heterostructures, which share a similar good ability to absorb the visible and near-infrared light, enabling them to be used in photocatalytic, photovoltaic, and optical devices [203]. The WS_2/GaN vdW heterobilayer structure exhibits significant optical absorption for the visible and near-ultraviolet light, which can be further improved by in-plane biaxial tensile and vertical uniaxial strain [204].

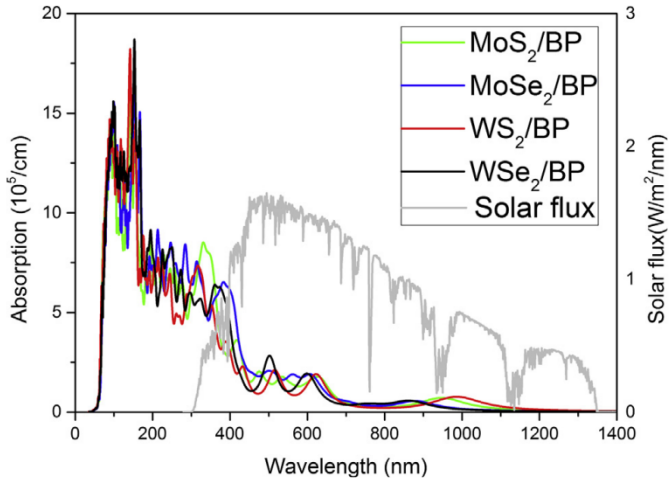

Figure 15. Optical-absorption coefficient of MoS_2/BP, $MoSe_2$/BP, WS_2/BP, and WSe_2/BP vdW heterostructures. (Reproduced with permission from ref. [203]. Copyright 2019 Elsevier Publications).

5.3. Optical Applications

The unique electronic and optoelectronic properties of heterostructures bring promising perspectives for the potential applications in the next generation of atomically thin electronic and optoelectronic devices such as LEDs [205], photodetectors [206–209], photovoltaics [129,133], and other innovative functional devices [202]. Recently, a vdW-integrated LED-based on monolayer WSe_2−CdS nanoribbon hybrid structure was demonstrated, and its structure is shown in Figure 16 [205]. Room temperature electrically driven light emission from monolayer WSe_2 was successfully achieved, with a turn-on voltage of ~2.0 V. By taking advantage of the CdS nanoribbon waveguide, the efficient optical routing of WSe_2 photoluminescence and electroluminescence emission was realized, showing great potential to interconnect with other functional optoelectronic units. A sub-band-gap photodetection in the MoS_2/2D Ruddlesden−Popper perovskite vdW heterojunction was obtained with a strong interlayer charge transfer caused by the type II energy band alignment (Figure 17) [210]. The reduced energy interval facilitates the photodetection ability in the near-infrared region, with the maximum photoresponsivity of 121 A W^{-1}, a detectivity of 4.3 × 10^{14} Jones at λ = 860 nm, and a rapid rise/decay (8.2/28.6 μs) time. The BP/$MoSi_2P_4$ heterostructure has promising prospects in optoelectronic devices such as solar cells due to its high stability and a typical type-II band alignment with a direct band gap, which can effectively facilitate the separation of photogenerated electron−hole pairs [211]. Based on the findings, the predicted photoelectric conversion efficiency for the BP/$MoSi_2P_4$ bilayers can reach 22.2%, which is larger than many other existing heterostructures. Two-dimensional materials-based heterostructures offer potential avenues for the continued development of novel photodetectors with broad spectral ranges. The various reported photodetectors based on different materials are summarized in Table 5.

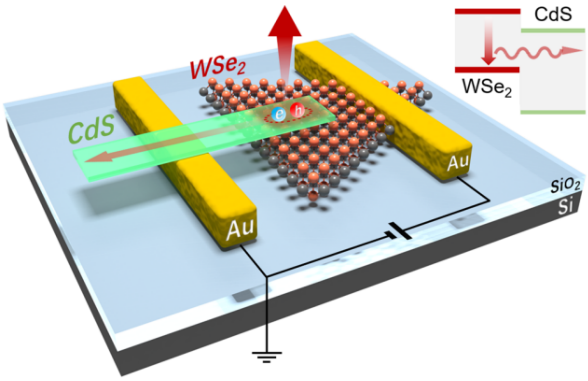

Figure 16. Schematic illustration of waveguide-integrated 2D LED based on monolayer WSe_2 and CdS nanoribbon p−n heterojunction. (Reproduced with permission from ref. [164]. Copyright 2022 ACS Publications).

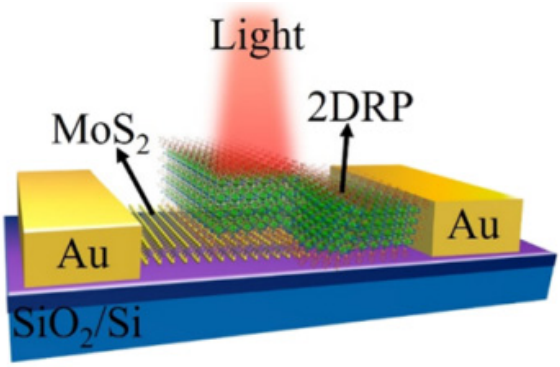

Figure 17. Schematic diagram of the photodetector fabricated from the MoS_2/2D Ruddlesden−Popper perovskite heterostructure. (Reproduced with permission from ref. [170]. Copyright 2022 ACS Publications).

Table 5. Comparison of the performances of photodetectors based on different materials.

Materials	Properties	Ref.
$GaTe/MoS_2$ p-n heterojunctions	Photoresponsivity: 1.36 A W^{-1} (at 633 nm); external quantum efficiency: 266%	[127]
Graphene/GaSe/WS_2/Graphene heterojunction	Photoresponsivity: 149 A W^{-1} (at 410 nm)	[212]
WS_2/Si heterojunction	Photoresponsivity: 224 mA W^{-1} (at 200–3043 nm)	[213]
InSe/Se heterojunction	Photoresponsivity: 110 mA W^{-1} (at 460 nm); external quantum efficiency: 8.7%	[206]
$PdSe_2/MoSe_2$ heterojunction	Photoresponsivity: 651 mA W^{-1} (at 532 nm)	[214]
InGaAs/SiO_2/graphene heterostructure	Photoresponsivity: 10^3 A W^{-1} (under weak light irradiation)	[215]
$VO_2/MoTe_2$ heterostructure	The heterostructure can realize 3 different functional modes: p-n junction mode, Schottky junction mode, and bolometer mode. Detection range: from visible light to longwave infrared radiation	[216]

6. Conclusions and Outlook

The discovery and development of 2D materials provides many exciting new chances for the exploration of high-performance optical devices. In this review, we introduced the properties as well as the fabrication methods of 2D materials and summarized their applications in the optoelectronics applications such as modulators, photodetectors, solar cells, and ultra-fast lasers. Hybrid integration with 2D materials can improve the performances of traditional optoelectronics devices, further expanding the application range of 2D materials; however, 2D materials-based optoelectronic devices have already achieved some milestone achievements. To realize industrial production, many problems still need to be considered and solved. First, convenient and cost-effective approaches should be explored to develop high-quality 2D material films. Second, many novel properties of 2D materials such as mechanical and magnetic properties remain to be further explored. Third, some high-performance 2D heterojunction materials or hybrid materials by the combination of the 2D materials and nanomaterials need further exploration and research. Fourth, the long-term operation stability of some optoelectronic devices in air needs to be enhanced as well, which plays a determining role for practical applications. Finally, researchers should delve into the mechanism of optoelectronic devices. The comprehensive understanding of optoelectronic devices will benefit the fabrication of high-performance devices. With continuous investigation, we believe that more and more practical optoelectronic devices with outstanding properties will emerge in the near future.

Author Contributions: Conceptualization, J.L. and H.L.; methodology, X.Y. and X.Z.; investigation, M.Z., Y.H., W.L. and C.W.; data curation, C.Z., R.Z. and B.L.; writing—original draft preparation, M.Z., Y.H., X.Y. and X.Z.; writing—review and editing, S.H.M.J., A.R. and R.P.; visualization, J.L.; funding acquisition, H.L. All authors have read and agreed to the published version of the manuscript.

Funding: This research was funded by Shandong Provincial Natural Science Foundation (Grant No.: ZR2021QE148, 2022HWYQ-060 and ZR2020ZD05); Guangdong Basic and Applied Basic Research Foundation (Grant No.: 2022A1515011473); National Natural Science Foundation of China (Grant No.: 51905306); Olle Engkvist (Grant No.: 211-0068); Swedish Research Council Formas (Grant No.: 2019-01538); and Qilu Young Scholar Program of Shandong University (Grant No.: 11500082063141).

Institutional Review Board Statement: Not applicable.

Informed Consent Statement: Not applicable.

Data Availability Statement: No new data were created or analyzed in this study. Data sharing is not applicable to this article.

Acknowledgments: Aimin Song from the University of Manchester is acknowledged for the helpful discussion on optoelectronic devices.

Conflicts of Interest: The authors declare no conflict of interest.

References

1. Avouris, P.; Dimitrakopoulos, C. Graphene: Synthesis and applications. *Mater. Today* **2012**, *15*, 86–97. [CrossRef]
2. Shim, J.; Park, H.Y.; Kang, D.H.; Kim, J.O.; Jo, S.H.; Park, Y.; Park, J.H. Electronic and Optoelectronic Devices based on Two-Dimensional Materials: From Fabrication to Application. *Adv. Electron. Mater.* **2017**, *3*, 1600364. [CrossRef]
3. Vu, Q.A.; Yu, W.J. Electronics and Optoelectronics Based on Two-Dimensional Materials. *J. Korean Phys. Soc.* **2018**, *73*, 1–15. [CrossRef]
4. Xu, M.; Liang, T.; Shi, M.; Chen, H. Graphene-like Two-Dimensional Materials. *Chem. Rev.* **2013**, *113*, 3766–3798. [CrossRef]
5. Wang, Q.H.; Kalantar-Zadeh, K.; Kis, A.; Coleman, J.N.; Strano, M.S. Electronics and optoelectronics of two-dimensional transition metal dichalcogenides. *Nat. Nanotechnol.* **2012**, *7*, 699–712. [CrossRef]
6. Mannix, A.J.; Kiraly, B.; Hersam, M.C.; Guisinger, N.P. Synthesis and chemistry of elemental 2D materials. *Nat. Rev. Chem.* **2017**, *1*, 0014. [CrossRef]
7. Khan, M.F.; Ahmed, F.; Rehman, S.; Akhtar, I.; Rehman, M.A.; Shinde, P.A.; Khan, K.; Kim, D.K.; Eom, J.; Lipsanen, H.; et al. High performance complementary WS2devices with hybrid Gr/Ni contacts. *Nanoscale* **2020**, *12*, 21280–21290. [CrossRef]
8. Xia, F.; Wang, H.; Xiao, D.; Dubey, M.; Ramasubramaniam, A. Two-dimensional material nanophotonics. *Nat. Photonics* **2014**, *8*, 899–907. [CrossRef]
9. Liu, M.; Yin, X.; Ulin-Avila, E.; Geng, B.; Zentgraf, T.; Ju, L.; Wang, F.; Zhang, X. A graphene-based broadband optical modulator. *Nature* **2011**, *474*, 64–67. [CrossRef] [PubMed]
10. Razaq, A.; Bibi, F.; Zheng, X.; Papadakis, R.; Jafri, S.H.M.; Li, H. Review on Graphene-, Graphene Oxide-, Reduced Graphene Oxide-Based Flexible Composites: From Fabrication to Applications. *Materials* **2022**, *15*, 1012. [CrossRef]
11. Eda, G.; Maier, S.A. Two-dimensional crystals: Managing light for optoelectronics. *ACS Nano* **2013**, *7*, 5660–5665. [CrossRef] [PubMed]
12. Liu, L.; Wu, L.; Wang, A.; Liu, H.; Ma, R.; Wu, K.; Chen, J.; Zhou, Z.; Tian, Y.; Yang, H.; et al. Ferroelectric-Gated InSe Photodetectors with High On/Off Ratios and Photoresponsivity. *Nano Lett.* **2020**, *20*, 6666–6673. [CrossRef] [PubMed]
13. Li, H.; Zhang, J.; Gholizadeh, A.B.; Brownless, J.; Fu, Y.; Cai, W.; Han, Y.; Duan, T.; Wang, Y.; Ling, H.; et al. Photoluminescent Semiconducting Graphene Nanoribbons via Longitudinally Unzipping Single-Walled Carbon Nanotubes. *ACS Appl. Mater. Interfaces* **2021**, *13*, 52892–52900. [CrossRef] [PubMed]
14. Khan, M.F.; Rehman, S.; Akhtar, I.; Aftab, S.; Ajmal, H.M.S.; Khan, W.; Kim, D.K.; Eom, J. High mobility $ReSe_2$ field effect transistors: Schottky-barrier-height-dependent photoresponsivity and broadband light detection with Co decoration. *2D Mater.* **2020**, *7*, 015010. [CrossRef]
15. Li, Y.; Fu, J.; Mao, X.; Chen, C.; Liu, H.; Gong, M.; Zeng, H. Enhanced bulk photovoltaic effect in two-dimensional ferroelectric $CuInP_2S_6$. *Nat. Commun.* **2021**, *12*, 5896. [CrossRef]
16. Mak, K.F.; Lee, C.; Hone, J.; Shan, J.; Heinz, T.F. Atomically thin MoS_2: A new direct-gap semiconductor. *Phys. Rev. Lett.* **2010**, *105*, 136805. [CrossRef]
17. Han, Y.; Li, H.; Jafri, S.H.M.; Ossipov, D.; Hilborn, J.; Leifer, K. Optimization and analysis of pyrene-maltose functionalized graphene surfaces for Con A detection. *Appl. Surf. Sci.* **2020**, *510*, 145409. [CrossRef]
18. Ishigami, M.; Chen, J.H.; Cullen, W.G.; Fuhrer, M.S.; Williams, E.D. Atomic structure of graphene on SiO_2. *Nano Lett.* **2007**, *7*, 1643–1648. [CrossRef]
19. Hwang, E.H.; Das Sarma, S. Dielectric function, screening, and plasmons in two-dimensional graphene. *Phys. Rev. B-Condens. Matter Mater. Phys.* **2007**, *75*, 205418. [CrossRef]
20. Nair, R.R.; Blake, P.; Grigorenko, A.N.; Novoselov, K.S.; Booth, T.J.; Stauber, T.; Peres, N.M.R.; Geim, A.K. Fine structure constant defines visual transparency of graphene. *Science* **2008**, *320*, 1308. [CrossRef]
21. Hiura, H.; Miyazaki, H.; Tsukagoshi, K. Determination of the number of graphene layers: Discrete distribution of the secondary electron intensity stemming from individual graphene layers. *Appl. Phys. Express* **2010**, *3*, 095101. [CrossRef]
22. Li, Z.Q.; Henriksen, E.A.; Jiang, Z.; Hao, Z.; Martin, M.C.; Kim, P.; Stormer, H.L.; Basov, D.N. Dirac charge dynamics in graphene by infrared spectroscopy. *Nat. Phys.* **2008**, *4*, 532–535. [CrossRef]
23. Mak, K.F.; Sfeir, M.Y.; Misewich, J.A.; Heinz, T.F. The evolution of electronic structure in few-layer graphene revealed by optical spectroscopy. *Proc. Natl. Acad. Sci. USA* **2010**, *107*, 14999–15004. [CrossRef] [PubMed]
24. Xing, G.; Guo, H.; Zhang, X.; Chien Sum, T.; Hon Alfred Huan, C.; Wang, F.; Zhang, Y.; Tian, C.; Girit, C.; Zettl, A.; et al. The Physics of ultrafast saturable absorption ingraphene. *Opt. Express* **2010**, *18*, 4564–4573. [CrossRef]
25. Zhang, H.; Virally, S.; Bao, Q.; Kian Ping, L.; Massar, S.; Godbout, N.; Kockaert, P. Z-Scan measurement of the nonlinear refractive index of graphene. *Opt. Lett.* **2012**, *37*, 1856–1858. [CrossRef]
26. Nandkishore, R.; Levitov, L. Polar Kerr effect and time reversal symmetry breaking in bilayer graphene. *Phys. Rev. Lett.* **2011**, *107*, 097402. [CrossRef]

27. Yang, H.; Feng, X.; Wang, Q.; Huang, H.; Chen, W.; Wee, A.T.S.; Ji, W. Giant two-photon absorption in bilayer graphene. *Nano Lett.* **2011**, *11*, 2622–2627. [CrossRef]
28. Bao, Q.; Zhang, H.; Wang, Y.; Ni, Z.; Yan, Y.; Shen, Z.X.; Loh, K.P.; Tang, D.Y. Atomic-layer craphene as a saturable absorber for ultrafast pulsed lasers. *Adv. Funct. Mater.* **2009**, *19*, 3077–3083. [CrossRef]
29. Luong, D.X.; Bets, K.V.; Algozeeb, W.A.; Stanford, M.G.; Kittrell, C.; Chen, W.; Salvatierra, R.V.; Ren, M.; McHugh, E.A.; Advincula, P.A.; et al. Gram-scale bottom-up flash graphene synthesis. *Nature* **2020**, *577*, 647–651. [CrossRef]
30. Bonaccorso, F.; Lombardo, A.; Hasan, T.; Sun, Z.; Colombo, L.; Ferrari, A.C. Production and processing of graphene and 2d crystals. *Mater. Today* **2012**, *15*, 564–589. [CrossRef]
31. Chen, T.; Sheng, Y.; Zhou, Y.; Chang, R.J.; Wang, X.; Huang, H.; Zhang, Q.; Hou, L.; Warner, J.H. High Photoresponsivity in Ultrathin 2D Lateral Graphene:WS_2:Graphene Photodetectors Using Direct CVD Growth. *ACS Appl. Mater. Interfaces* **2019**, *11*, 6421–6430. [CrossRef] [PubMed]
32. Zhuo, L.; Fan, P.; Zhang, S.; Liu, X.; Guo, X.; Zhang, Y.; Zhan, Y.; Li, D.; Che, Z.; Zhu, W.; et al. A broadband all-fiber integrated graphene photodetector with CNT-enhanced responsivity. *Nanoscale* **2020**, *12*, 14188–14193. [CrossRef]
33. Ahn, S.; Chung, H.; Chen, W.; Moreno-Gonzalez, M.A.; Vazquez-Mena, O. Optoelectronic response of hybrid PbS-QD/graphene photodetectors. *J. Chem. Phys.* **2019**, *151*, 234705. [CrossRef] [PubMed]
34. Koo, D.; Jung, S.; Seo, J.; Jeong, G.; Choi, Y.; Lee, J.; Lee, S.M.; Cho, Y.; Jeong, M.; Lee, J.; et al. Flexible Organic Solar Cells Over 15% Efficiency with Polyimide-Integrated Graphene Electrodes. *Joule* **2020**, *4*, 1021–1034. [CrossRef]
35. Yu, S.; Zhao, L.; Liu, R.; Zhang, C.; Zheng, H.; Sun, Y.; Li, L. Performance enhancement of Cu-based AZO multilayer thin films via graphene fence engineering for organic solar cells. *Sol. Energy Mater. Sol. Cells* **2018**, *183*, 66–72. [CrossRef]
36. Kumar, M.R. A Compact Graphene Based Nano-Antenna for Communication in Nano-Network. *J. Inst. Electron. Comput.* **2019**, *1*, 17–27. [CrossRef]
37. Biswas, R.V.; Arifin, F. Design and Analysis of a Graphene Based Slotted Bowtie Optical Plasmonic Nanoantenna. *Res. Square* **2021**. [CrossRef]
38. Ye, L.; Sui, K.; Zhang, Y.; Liu, Q.H. Broadband optical waveguide modulators based on strongly coupled hybrid graphene and metal nanoribbons for near-infrared applications. *Nanoscale* **2019**, *11*, 3154–3163. [CrossRef] [PubMed]
39. Maier, M.; Nemilentsau, A.; Low, T.; Luskin, M. Ultracompact Amplitude Modulator by Coupling Hyperbolic Polaritons over a Graphene-Covered Gap. *ACS Photonics* **2018**, *5*, 544–551. [CrossRef]
40. Li, H.; Papadakis, R.; Hussain, T.; Karton, A.; Liu, J. Moiré patterns arising from bilayer graphone/graphene superlattice. *Nano Res.* **2020**, *13*, 1060–1064. [CrossRef]
41. Mueller, T.; Xia, F.; Avouris, P. Graphene photodetectors for high-speed optical communications. *Nat. Photonics* **2010**, *4*, 297–301. [CrossRef]
42. Ding, Y.; Cheng, Z.; Zhu, X.; Yvind, K.; Dong, J.; Galili, M.; Hu, H.; Mortensen, N.A.; Xiao, S.; Oxenløwe, L.K. Ultra-compact integrated graphene plasmonic photodetector with bandwidth above 110 GHz. *Nanophotonics* **2020**, *9*, 317–325. [CrossRef]
43. Guo, J.; Li, J.; Liu, C.; Yin, Y.; Wang, W.; Ni, Z.; Fu, Z.; Yu, H.; Xu, Y.; Shi, Y.; et al. High-performance silicon−graphene hybrid plasmonic waveguide photodetectors beyond 1.55 µm. *Light Sci. Appl.* **2020**, *9*, 29. [CrossRef] [PubMed]
44. Ricciardulli, A.G.; Yang, S.; Feng, X.; Blom, P.W.M. Solution-Processable High-Quality Graphene for Organic Solar Cells. *ACS Appl. Mater. Interfaces* **2017**, *9*, 25412–25417. [CrossRef] [PubMed]
45. Mahmoudi, T.; Wang, Y.; Hahn, Y.B. Graphene and its derivatives for solar cells application. *Nano Energy* **2018**, *47*, 51–65. [CrossRef]
46. Li, X.; Zhu, H.; Wang, K.; Cao, A.; Wei, J.; Li, C.; Jia, Y.; Li, Z.; Li, X.; Wu, D. Graphene-on-silicon schottky junction solar cells. *Adv. Mater.* **2010**, *22*, 2743–2748. [CrossRef] [PubMed]
47. Liu, Z.; Li, J.; Yan, F. Package-free flexible organic solar cells with graphene top electrodes. *Adv. Mater.* **2013**, *25*, 4296–4301. [CrossRef] [PubMed]
48. Hilal, M.; Han, J.I. Significant improvement in the photovoltaic stability of bulk heterojunction organic solar cells by the molecular level interaction of graphene oxide with a PEDOT: PSS composite hole transport layer. *Sol. Energy* **2018**, *167*, 24–34. [CrossRef]
49. Liu, N.; Langguth, L.; Weiss, T.; Kästel, J.; Fleischhauer, M.; Pfau, T.; Giessen, H. Plasmonic analogue of electromagnetically induced transparency at the Drude damping limit. *Nat. Mater.* **2009**, *8*, 758–762. [CrossRef] [PubMed]
50. Ullah, Z.; Witjaksono, G.; Nawi, I.; Tansu, N.; Khattak, M.I.; Junaid, M. A review on the development of tunable graphene nanoantennas for terahertz optoelectronic and plasmonic applications. *Sensors* **2020**, *20*, 1401. [CrossRef] [PubMed]
51. Aieta, F.; Genevet, P.; Kats, M.; Capasso, F. Aberrations of flat lenses and aplanatic metasurfaces. *Opt. Express* **2013**, *21*, 31530. [CrossRef]
52. Nagatsuma, T.; Ducournau, G.; Renaud, C.C. Advances in terahertz communications accelerated by photonics. *Nat. Photonics* **2016**, *10*, 371–379. [CrossRef]
53. Yoon, H.J.; Jun, D.H.; Yang, J.H.; Zhou, Z.; Yang, S.S.; Cheng, M.M.C. Carbon dioxide gas sensor using a graphene sheet. *Sens. Actuators B Chem.* **2011**, *157*, 310–313. [CrossRef]
54. Cox, J.D.; García De Abajo, F.J. Nonlinear Graphene Nanoplasmonics. *Acc. Chem. Res.* **2019**, *52*, 2536–2547. [CrossRef] [PubMed]
55. Carrasco, E.; Perruisseau-Carrier, J. Reflectarray antenna at terahertz using graphene. *IEEE Antennas Wirel. Propag. Lett.* **2013**, *12*, 253–256. [CrossRef]

56. Moradi, K.; Pourziad, A.; Nikmehr, S. A frequency reconfigurable microstrip antenna based on graphene in Terahertz Regime. *Optik* **2021**, *228*, 166201. [CrossRef]
57. Esquius-Morote, M.; Gomez-Diaz, J.S.; Perruisseau-Carrier, J. Sinusoidally modulated graphene leaky-wave antenna for electronic beamscanning at THz. *IEEE Trans. Terahertz Sci. Technol.* **2014**, *4*, 116–122. [CrossRef]
58. Fuscaldo, W.; Burghignoli, P.; Baccarelli, P.; Galli, A. Graphene fabry-perot cavity leaky-wave antennas: Plasmonic versus nonplasmonic solutions. *IEEE Trans. Antennas Propag.* **2017**, *65*, 1651–1660. [CrossRef]
59. Dash, S.; Patnaik, A. Performance of Graphene Plasmonic Antenna in Comparison with Their Counterparts for Low-Terahertz Applications. *Plasmonics* **2018**, *13*, 2353–2360. [CrossRef]
60. Liang, G.; Hu, X.; Yu, X.; Shen, Y.; Li, L.H.; Davies, A.G.; Linfield, E.H.; Liang, H.K.; Zhang, Y.; Yu, S.F.; et al. Integrated Terahertz Graphene Modulator with 100% Modulation Depth. *ACS Photonics* **2015**, *2*, 1559–1566. [CrossRef]
61. Youngblood, N.; Anugrah, Y.; Ma, R.; Koester, S.J.; Li, M. Multifunctional graphene optical modulator and photodetector integrated on silicon waveguides. *Nano Lett.* **2014**, *14*, 2741–2746. [CrossRef] [PubMed]
62. Phare, C.T.; Daniel Lee, Y.H.; Cardenas, J.; Lipson, M. Graphene electro-optic modulator with 30 GHz bandwidth. *Nat. Photonics* **2015**, *9*, 511–514. [CrossRef]
63. Zhong, C.; Li, J.; Lin, H. Graphene-based all-optical modulators. *Front. Optoelectron.* **2020**, *13*, 114–128. [CrossRef]
64. Chi, J.; Liu, H.; Huang, N.; Wang, Z. A broadband enhanced plasmonic modulator based on double-layer graphene at mid-infrared wavelength. *J. Phys. D Appl. Phys.* **2019**, *52*, 445101. [CrossRef]
65. Haider, G.; Ravindranath, R.; Chen, T.P.; Roy, P.; Roy, P.K.; Cai, S.Y.; Chang, H.T.; Chen, Y.F. Dirac point induced ultralow-threshold laser and giant optoelectronic quantum oscillations in graphene-based heterojunctions. *Nat. Commun.* **2017**, *8*, 256. [CrossRef] [PubMed]
66. Sobon, G.; Sotor, J.; Przewolka, A.; Pasternak, I.; Strupinski, W.; Abramski, K. Amplification of noise-like pulses generated from a graphene-based Tm-doped all-fiber laser. *Opt. Express* **2016**, *24*, 20359. [CrossRef] [PubMed]
67. Wang, J.; Song, J.; Mu, X.; Sun, M. Optoelectronic and photoelectric properties and applications of graphene-based nanostructures. *Mater. Today Phys.* **2020**, *13*, 100196. [CrossRef]
68. Chakraborty, O.S.; Marshall, P.; Folland, T.G.; Kim, Y.-J.; Novoselov, K.S. Gain modulation by grapheneplasmons in aperiodic lattice lasers. *Science* **2016**, *351*, 241–246. [CrossRef]
69. Polini, M. Applied optics: Tuning terahertz lasers via graphene plasmons. *Science* **2016**, *351*, 229–230. [CrossRef] [PubMed]
70. Elahi, E.; Khan, M.F.; Rehman, S.; Khalil, H.M.W.; Rehman, M.A.; Kim, D.K.; Kim, H.; Khan, K.; Shahzad, M.; Iqbal, M.W.; et al. Enhanced electrical and broad spectral (UV-Vis-NIR) photodetection in a Gr/$ReSe_2$/Gr heterojunction. *Dalt. Trans.* **2020**, *49*, 10017–10027. [CrossRef]
71. Radisavljevic, B.; Radenovic, A.; Brivio, J.; Giacometti, V.; Kis, A. Single-layer MoS_2 transistors. *Nat. Nanotechnol.* **2011**, *6*, 147–150. [CrossRef] [PubMed]
72. Chhowalla, M.; Shin, H.S.; Eda, G.; Li, L.J.; Loh, K.P.; Zhang, H. The chemistry of two-dimensional layered transition metal dichalcogenide nanosheets. *Nat. Chem.* **2013**, *5*, 263–275. [CrossRef] [PubMed]
73. Eda, G.; Yamaguchi, H.; Voiry, D.; Fujita, T.; Chen, M.; Chhowalla, M. Photoluminescence from chemically exfoliated MoS_2. *Nano Lett.* **2011**, *11*, 5111–5116. [CrossRef] [PubMed]
74. Ding, Y.; Wang, Y.; Ni, J.; Shi, L.; Shi, S.; Tang, W. First principles study of structural, vibrational and electronic properties of graphene-like MX_2 (M=Mo, Nb, W, Ta; X=S, Se, Te) monolayers. *Phys. B Condens. Matter* **2011**, *406*, 2254–2260. [CrossRef]
75. Yun, W.S.; Han, S.W.; Hong, S.C.; Kim, I.G.; Lee, J.D. Thickness and strain effects on electronic structures of transition metal dichalcogenides: 2H-MX_2 semiconductors (M = Mo, W; X = S, Se, Te). *Phys. Rev. B-Condens. Matter Mater. Phys.* **2012**, *85*, 033305. [CrossRef]
76. Xia, C.; Li, J. Recent advances in optoelectronic properties and applications of two-dimensional metal chalcogenides. *J. Semicond.* **2016**, *37*, 051001. [CrossRef]
77. Liu, L.; Wang, H.; Wu, Q.; Wu, K.; Tian, Y.; Yang, H.; Shen, C.M.; Bao, L.; Qin, Z.; Gao, H.J. Ferroelectric-gated ReS_2 field-effect transistors for nonvolatile memory. *Nano Res.* **2022**, *15*, 5443–5449. [CrossRef]
78. Hui, Y.Y.; Liu, X.; Jie, W.; Chan, N.Y.; Hao, J.; Hsu, Y.T.; Li, L.J.; Guo, W.; Lau, S.P. Exceptional tunability of band energy in a compressively strained trilayer MoS_2 sheet. *ACS Nano* **2013**, *7*, 7126–7131. [CrossRef]
79. Mouri, S.; Miyauchi, Y.; Matsuda, K. Tunable photoluminescence of monolayer MoS_2 via chemical doping. *Nano Lett.* **2013**, *13*, 5944–5948. [CrossRef]
80. Brent, J.R.; Savjani, N.; O'Brien, P. Synthetic approaches to two-dimensional transition metal dichalcogenide nanosheets. *Prog. Mater. Sci.* **2017**, *89*, 411–478. [CrossRef]
81. Yao, J.D.; Zheng, Z.Q.; Yang, G.W. Production of large-area 2D materials for high-performance photodetectors by pulsed-laser deposition. *Prog. Mater. Sci.* **2019**, *106*, 100573. [CrossRef]
82. Zhou, J.; Lin, J.; Huang, X.; Zhou, Y.; Chen, Y.; Xia, J.; Wang, H.; Xie, Y.; Yu, H.; Lei, J.; et al. A library of atomically thin metal chalcogenides. *Nature* **2018**, *556*, 355–359. [CrossRef] [PubMed]
83. Sahu, R. Two-Dimensional MoS_2 and Heterostructure Growth by Pulsed Laser Deposition. *Mod. Concept. Mater. Sci.* **2019**, *2*, 000534. [CrossRef]
84. Loh, T.A.J.; Chua, D.H.C.; Wee, A.T.S. One-step Synthesis of Few-layer WS_2 by Pulsed Laser Deposition. *Sci. Rep.* **2015**, *5*, 18116. [CrossRef]

85. Serrao, C.R.; Diamond, A.M.; Hsu, S.L.; You, L.; Gadgil, S.; Clarkson, J.; Carraro, C.; Maboudian, R.; Hu, C.; Salahuddin, S. Highly crystalline MoS_2 thin films grown by pulsed laser deposition. *Appl. Phys. Lett.* **2015**, *106*, 052101. [CrossRef]
86. Chen, X.; Shehzad, K.; Gao, L.; Long, M.; Guo, H.; Qin, S.; Wang, X.; Wang, F.; Shi, Y.; Hu, W.; et al. Graphene Hybrid Structures for Integrated and Flexible Optoelectronics. *Adv. Mater.* **2020**, *32*, 1902039. [CrossRef] [PubMed]
87. Wu, M.; Xiao, Y.; Zeng, Y.; Zhou, Y.; Zeng, X.; Zhang, L.; Liao, W. Synthesis of two-dimensional transition metal dichalcogenides for electronics and optoelectronics. *InfoMat* **2021**, *3*, 362–396. [CrossRef]
88. Lien, D.-H.; Kang, J.S.; Amani, M.; Chen, K.; Tosun, M.; Wang, H.-P.; Roy, T.; Eggleston, M.; Wu, M.C.; Dubey, M.; et al. Engineering Light Outcoupling in 2D Materials. *Nano Lett.* **2015**, *15*, 1356–1361. [CrossRef] [PubMed]
89. Lien, D.H.; Amani, M.; Desai, S.B.; Ahn, G.H.; Han, K.; He, J.H.; Ager, J.W.; Wu, M.C.; Javey, A. Large-area and bright pulsed electroluminescence in monolayer semiconductors. *Nat. Commun.* **2018**, *9*, 1229. [CrossRef] [PubMed]
90. Withers, F.; Del Pozo-Zamudio, O.; Mishchenko, A.; Rooney, A.P.; Gholinia, A.; Watanabe, K.; Taniguchi, T.; Haigh, S.J.; Geim, A.K.; Tartakovskii, A.I.; et al. Light-emitting diodes by band-structure engineering in van der Waals heterostructures. *Nat. Mater.* **2015**, *14*, 301–306. [CrossRef] [PubMed]
91. Kim, H.C.; Kim, H.; Lee, J.U.; Lee, H.B.; Choi, D.H.; Lee, J.H.; Lee, W.H.; Jhang, S.H.; Park, B.H.; Cheong, H.; et al. Engineering Optical and Electronic Properties of WS_2 by Varying the Number of Layers. *ACS Nano* **2015**, *9*, 6854–6860. [CrossRef] [PubMed]
92. Cheng, R.; Li, D.; Zhou, H.; Wang, C.; Yin, A.; Jiang, S.; Liu, Y.; Chen, Y.; Huang, Y.; Duan, X. Electroluminescence and photocurrent generation from atomically sharp WSe_2/MoS_2 heterojunction p-n diodes. *Nano Lett.* **2014**, *14*, 5590–5597. [CrossRef]
93. Baugher, B.W.H.; Churchill, H.O.H.; Yang, Y.; Jarillo-Herrero, P. Optoelectronic devices based on electrically tunable p-n diodes in a monolayer dichalcogenide. *Nat. Nanotechnol.* **2014**, *9*, 262–267. [CrossRef] [PubMed]
94. Ross, J.S.; Klement, P.; Jones, A.M.; Ghimire, N.J.; Yan, J.; Mandrus, D.G.; Taniguchi, T.; Watanabe, K.; Kitamura, K.; Yao, W.; et al. Electrically tunable excitonic light-emitting diodes based on monolayer WSe_2 p-n junctions. *Nat. Nanotechnol.* **2014**, *9*, 268–272. [CrossRef] [PubMed]
95. Pospischil, A.; Furchi, M.M.; Mueller, T. Solar-energy conversion and light emission in an atomic monolayer p-n diode. *Nat. Nanotechnol.* **2014**, *9*, 257–261. [CrossRef] [PubMed]
96. Sundaram, R.S.; Engel, M.; Lombardo, A.; Krupke, R.; Ferrari, A.C.; Avouris, P.; Steiner, M. Electroluminescence in single layer MoS_2. *Nano Lett.* **2013**, *13*, 1416–1421. [CrossRef] [PubMed]
97. Bernardi, M.; Palummo, M.; Grossman, J.C. Extraordinary sunlight absorption and one nanometer thick photovoltaics using two-dimensional monolayer materials. *Nano Lett.* **2013**, *13*, 3664–3670. [CrossRef] [PubMed]
98. Polman, A.; Atwater, H.A. Photonic design principles for ultrahigh-efficiency photovoltaics. *Nat. Mater.* **2012**, *11*, 174–177. [CrossRef] [PubMed]
99. Ponraj, J.S.; Xu, Z.Q.; Dhanabalan, S.C.; Mu, H.; Wang, Y.; Yuan, J.; Li, P.; Thakur, S.; Ashrafi, M.; McCoubrey, K.; et al. Photonics and optoelectronics of two-dimensional materials beyond graphene. *Nanotechnology* **2016**, *27*, 462001. [CrossRef]
100. Antolín, E.; Svatek, S.A.; Bueno-Blanco, C.; Martí, A.; Lin, D.-Y.; Rodríguez-Peña, M.; Luna, M. MoS_2 solar cell with 120 nm-absorber and 3.8% AM1.5G efficiency. In Proceedings of the 49th IEEE Photovoltaic Specialists Conference, Philadelphia, PA, USA, 5–10 June 2022.
101. Bin Rafiq, M.K.S.; Amin, N.; Alharbi, H.F.; Luqman, M.; Ayob, A.; Alharthi, Y.S.; Alharthi, N.H.; Bais, B.; Akhtaruzzaman, M. WS_2: A New Window Layer Material for Solar Cell Application. *Sci. Rep.* **2020**, *10*, 771. [CrossRef] [PubMed]
102. Shin, D.H.; Jang, C.W.; Ko, J.S.; Choi, S.H. Enhancement of efficiency and stability in organic solar cells by employing MoS_2 transport layer, graphene electrode, and graphene quantum dots-added active layer. *Appl. Surf. Sci.* **2021**, *538*, 148155. [CrossRef]
103. Flöry, N.; Ma, P.; Salamin, Y.; Emboras, A.; Taniguchi, T.; Watanabe, K.; Leuthold, J.; Novotny, L. Waveguide-integrated van der Waals heterostructure photodetector at telecom wavelengths with high speed and high responsivity. *Nat. Nanotechnol.* **2020**, *15*, 118–124. [CrossRef] [PubMed]
104. Varghese, A.; Saha, D.; Thakar, K.; Jindal, V.; Ghosh, S.; Medhekar, N.V.; Ghosh, S.; Lodha, S. Near-Direct Bandgap WSe_2/ReS_2 Type-II pn Heterojunction for Enhanced Ultrafast Photodetection and High-Performance Photovoltaics. *Nano Lett.* **2020**, *20*, 1707–1717. [CrossRef] [PubMed]
105. Wang, X.; Cui, Y.; Li, T.; Lei, M.; Li, J.; Wei, Z. Recent Advances in the Functional 2D Photonic and Optoelectronic Devices. *Adv. Opt. Mater.* **2019**, *7*, 1801274. [CrossRef]
106. Wei, X.; Yan, F.; Lv, Q.; Shen, C.; Wang, K. Fast gate-tunable photodetection in the graphene sandwiched WSe_2/GaSe heterojunctions. *Nanoscale* **2017**, *9*, 8388–8392. [CrossRef] [PubMed]
107. Thakar, K.; Mukherjee, B.; Grover, S.; Kaushik, N.; Deshmukh, M.; Lodha, S. Multilayer ReS_2 Photodetectors with Gate Tunability for High Responsivity and High-Speed Applications. *ACS Appl. Mater. Interfaces* **2018**, *10*, 36512–36522. [CrossRef] [PubMed]
108. Li, X.; Zuo, X.; Li, H.; Han, L.; Gao, Q.; Li, D.; Cui, B.; Liu, D.; Qu, F. Exotic magnetism in As-doped α/β-In_2Se_3 monolayers with tunable anisotropic carrier mobility. *Phys. Chem. Chem. Phys.* **2019**, *21*, 19234–19241. [CrossRef] [PubMed]
109. Zhao, C.; Sekhar, M.C.; Lu, W.; Zhang, C.; Lai, J.; Jia, S.; Sun, D. Anisotropic visible photoluminescence from thermally annealed few-layer black phosphorus. *Nanotechnology* **2018**, *29*, 245202. [CrossRef] [PubMed]
110. Sim, S.; Lee, D.; Trifonov, A.V.; Kim, T.; Cha, S.; Sung, J.H.; Cho, S.; Shim, W.; Jo, M.H.; Choi, H. Ultrafast quantum beats of anisotropic excitons in atomically thin ReS_2. *Nat. Commun.* **2018**, *9*, 351. [CrossRef] [PubMed]
111. Kufer, D.; Konstantatos, G. Highly Sensitive, Encapsulated MoS_2 Photodetector with Gate Controllable Gain and Speed. *Nano Lett.* **2015**, *15*, 7307–7313. [CrossRef] [PubMed]

112. Liu, E.; Long, M.; Zeng, J.; Luo, W.; Wang, Y.; Pan, Y.; Zhou, W.; Wang, B.; Hu, W.; Ni, Z.; et al. High Responsivity Phototransistors Based on Few-Layer ReS_2 for Weak Signal Detection. *Adv. Funct. Mater.* **2016**, *26*, 1938–1944. [CrossRef]
113. Qin, J.K.; Ren, D.D.; Shao, W.Z.; Li, Y.; Miao, P.; Sun, Z.Y.; Hu, P.; Zhen, L.; Xu, C.Y. Photoresponse Enhancement in Monolayer ReS2 Phototransistor Decorated with CdSe-CdS-ZnS Quantum Dots. *ACS Appl. Mater. Interfaces* **2017**, *9*, 39456–39463. [CrossRef] [PubMed]
114. Zhang, K.; Fang, X.; Wang, Y.; Wan, Y.; Song, Q.; Zhai, W.; Li, Y.; Ran, G.; Ye, Y.; Dai, L. Ultrasensitive Near-Infrared Photodetectors Based on a Graphene-$MoTe_2$-Graphene Vertical van der Waals Heterostructure. *ACS Appl. Mater. Interfaces* **2017**, *9*, 5392–5398. [CrossRef]
115. Yang, T.; Zheng, B.; Wang, Z.; Xu, T.; Pan, C.; Zou, J.; Zhang, X.; Qi, Z.; Liu, H.; Feng, Y.; et al. Van der Waals epitaxial growth and optoelectronics of large-scale WSe_2/SnS_2 vertical bilayer p-n junctions. *Nat. Commun.* **2017**, *8*, 1906. [CrossRef] [PubMed]
116. Zhou, X.; Hu, X.; Zhou, S.; Song, H.; Zhang, Q.; Pi, L.; Li, L.; Li, H.; Lü, J.; Zhai, T. Tunneling Diode Based on WSe_2/SnS_2 Heterostructure Incorporating High Detectivity and Responsivity. *Adv. Mater.* **2018**, *30*, 1703286. [CrossRef] [PubMed]
117. Özdemir, O.; Ramiro, I.; Gupta, S.; Konstantatos, G. High Sensitivity Hybrid PbS CQD-TMDC Photodetectors up to 2 µm. *ACS Photonics* **2019**, *6*, 2381–2386. [CrossRef]
118. Zhang, S.; Wang, X.; Chen, Y.; Wu, G.; Tang, Y.; Zhu, L.; Wang, H.; Jiang, W.; Sun, L.; Lin, T.; et al. Ultrasensitive Hybrid MoS_2-ZnCdSe Quantum Dot Photodetectors with High Gain. *ACS Appl. Mater. Interfaces* **2019**, *11*, 23667–23672. [CrossRef] [PubMed]
119. Schneider, D.S.; Schneider, D.S.; Grundmann, A.; Bablich, A.; Passi, V.; Passi, V.; Kataria, S.; Kalisch, H.; Heuken, M.; Heuken, M.; et al. Highly Responsive Flexible Photodetectors Based on MOVPE Grown Uniform Few-Layer MoS_2. *ACS Photonics* **2020**, *7*, 1388–1395. [CrossRef]
120. Li, L.; Shang, Y.; Lv, S.; Li, Y.; Fang, Y.; Li, H. Flexible and highly responsive photodetectors based on heterostructures of MoS_2 and all-carbon transistors. *Nanotechnology* **2021**, *32*, 315209. [CrossRef]
121. Fang, F.; Wan, Y.; Li, H.; Fang, S.; Huang, F.; Zhou, B.; Jiang, K.; Tung, V.; Li, L.J.; Shi, Y. Two-Dimensional $Cs_2AgBiBr_6/WS_2$Heterostructure-Based Photodetector with Boosted Detectivity via Interfacial Engineering. *ACS Nano* **2022**, *16*, 3985–3993. [CrossRef]
122. Ni, Z.; Ma, L.; Du, S.; Xu, Y.; Yuan, M.; Fang, H.; Wang, Z.; Xu, M.; Li, D.; Yang, J.; et al. Plasmonic Silicon Quantum Dots Enabled High-Sensitivity Ultrabroadband Photodetection of Graphene-Based Hybrid Phototransistors. *ACS Nano* **2017**, *11*, 9854–9862. [CrossRef] [PubMed]
123. Liu, X.; Luo, X.; Nan, H.; Guo, H.; Wang, P.; Zhang, L.; Zhou, M.; Yang, Z.; Shi, Y.; Hu, W.; et al. Epitaxial Ultrathin Organic Crystals on Graphene for High-Efficiency Phototransistors. *Adv. Mater.* **2016**, *28*, 5200–5205. [CrossRef] [PubMed]
124. Zhang, Y.; Ye, J.; Matsuhashi, Y.; Iwasa, Y. Ambipolar MoS_2 thin flake transistors. *Nano Lett.* **2012**, *12*, 1136–1140. [CrossRef] [PubMed]
125. Yin, Z.; Li, H.; Li, H.; Jiang, L.; Shi, Y.; Sun, Y.; Lu, G.; Zhang, Q.; Chen, X.; Zhang, H. Single-layer MoS_2 phototransistors. *ACS Nano* **2012**, *6*, 74–80. [CrossRef] [PubMed]
126. Zhou, X.; Zhou, N.; Li, C.; Song, H.; Zhang, Q.; Hu, X.; Gan, L.; Li, H.; Lü, J.; Luo, J.; et al. Vertical heterostructures based on $SnSe_2/MoS_2$ for high performance photodetectors. *2D Mater.* **2017**, *4*, 025048. [CrossRef]
127. Yang, S.; Wang, C.; Ataca, C.; Li, Y.; Chen, H.; Cai, H.; Suslu, A.; Grossman, J.C.; Jiang, C.; Liu, Q.; et al. Self-Driven Photodetector and Ambipolar Transistor in Atomically Thin GaTe-MoS_2 p-n vdW Heterostructure. *ACS Appl. Mater. Interfaces* **2016**, *8*, 2533–2539. [CrossRef]
128. Yang, J.; Qin, H.; Zhang, K. Emerging terahertz photodetectors based on two-dimensional materials. *Opt. Commun.* **2018**, *406*, 36–43. [CrossRef]
129. Castellanos-Gomez, A.; Vicarelli, L.; Prada, E.; Island, J.O.; Narasimha-Acharya, K.L.; Blanter, S.I.; Groenendijk, D.J.; Buscema, M.; Steele, G.A.; Alvarez, J.V.; et al. Isolation and characterization of few-layer black phosphorus. *2D Mater.* **2014**, *1*, 025001. [CrossRef]
130. Cartz, L.; Srinivasa, S.R.; Riedner, R.J.; Jorgensen, J.D.; Worlton, T.G. Effect of pressure on bonding in black phosphorus. *J. Chem. Phys.* **1979**, *71*, 1718–1721. [CrossRef]
131. Li, L.; Yu, Y.; Ye, G.J.; Ge, Q.; Ou, X.; Wu, H.; Feng, D.; Chen, X.H.; Zhang, Y. Black phosphorus field-effect transistors. *Nat. Nanotechnol.* **2014**, *9*, 372–377. [CrossRef] [PubMed]
132. Jones, A.M.; Yu, H.; Ross, J.S.; Klement, P.; Ghimire, N.J.; Yan, J.; Mandrus, D.G.; Yao, W.; Xu, X. Spin-layer locking effects in optical orientation of exciton spin in bilayer WSe_2. *Nat. Phys.* **2014**, *10*, 130–134. [CrossRef]
133. Li, C.; Cao, Q.; Wang, F.; Xiao, Y.; Li, Y.; Delaunay, J.J.; Zhu, H. Engineering graphene and TMDs based van der Waals heterostructures for photovoltaic and photoelectrochemical solar energy conversion. *Chem. Soc. Rev.* **2018**, *47*, 4981–5037. [CrossRef] [PubMed]
134. Splendiani, A.; Sun, L.; Zhang, Y.; Li, T.; Kim, J.; Chim, C.Y.; Galli, G.; Wang, F. Emerging photoluminescence in monolayer MoS_2. *Nano Lett.* **2010**, *10*, 1271–1275. [CrossRef] [PubMed]
135. Sofer, Z.; Sedmidubský, D.; Huber, Š.; Luxa, J.; Bouša, D.; Boothroyd, C.; Pumera, M. Layered Black Phosphorus: Strongly Anisotropic Magnetic, Electronic, and Electron-Transfer Properties. *Angew. Chem.* **2016**, *128*, 3443–3447. [CrossRef]
136. Xia, F.; Wang, H.; Jia, Y. Rediscovering black phosphorus as an anisotropic layered material for optoelectronics and electronics. *Nat. Commun.* **2014**, *5*, 4458. [CrossRef] [PubMed]

137. Lu, S.B.; Miao, L.L.; Guo, Z.N.; Qi, X.; Zhao, C.J.; Zhang, H.; Wen, S.C.; Tang, D.Y.; Fan, D.Y. Broadband nonlinear optical response in multi-layer black phosphorus: An emerging infrared and mid-infrared optical material. *Opt. Express* **2015**, *23*, 11183. [CrossRef]
138. Debnath, P.C.; Park, K.; Song, Y.-W. Recent Advances in Black-Phosphorus-Based Photonics and Optoelectronics Devices. *Small Methods* **2018**, *2*, 1700315. [CrossRef]
139. Xu, Y.; Liu, C.; Guo, C.; Yu, Q.; Guo, W.; Lu, W.; Chen, X.; Wang, L.; Zhang, K. High performance near infrared photodetector based on in-plane black phosphorus p-n homojunction. *Nano Energy* **2020**, *70*, 104518. [CrossRef]
140. Ma, Y.; Dong, B.; Wei, J.; Chang, Y.; Huang, L.; Ang, K.W.; Lee, C. High-Responsivity Mid-Infrared Black Phosphorus Slow Light Waveguide Photodetector. *Adv. Opt. Mater.* **2020**, *8*, 2000337. [CrossRef]
141. Huang, L.; Dong, B.; Guo, X.; Chang, Y.; Chen, N.; Huang, X.; Liao, W.; Zhu, C.; Wang, H.; Lee, C.; et al. Waveguide-Integrated Black Phosphorus Photodetector for Mid-Infrared Applications. *ACS Nano* **2019**, *13*, 913–921. [CrossRef]
142. Jiao, H.; Wang, X.; Chen, Y.; Guo, S.; Wu, S.; Song, C.; Huang, S.; Huang, X.; Tai, X.; Lin, T.; et al. HgCdTe/black phosphorus van der Waals heterojunction for high-performance polarization-sensitive midwave infrared photodetector. *Sci. Adv.* **2022**, *8*, eabn1811. [CrossRef] [PubMed]
143. Zhu, W.; Wei, X.; Yan, F.; Lv, Q.; Hu, C.; Wang, K. Broadband polarized photodetector based on p-BP/n-ReS_2 heterojunction. *J. Semicond.* **2019**, *40*, 092001. [CrossRef]
144. Zhang, M.; Wu, Q.; Zhang, F.; Chen, L.; Jin, X.; Hu, Y.; Zheng, Z.; Zhang, H. 2D Black Phosphorus Saturable Absorbers for Ultrafast Photonics. *Adv. Opt. Mater.* **2019**, *7*, 1800224. [CrossRef]
145. Zhu, Y.; Tang, B.; Jiang, C. Tunable ultra-broadband anisotropic absorbers based on multi-layer black phosphorus ribbons. *Appl. Phys. Express* **2019**, *12*, 032009. [CrossRef]
146. Matsuno, Y.; Nagumo, N.; Araki, M.; Yada, K.; Yamaga, K.; Sakurai, A. Non-equilibrium mid-infrared black phosphorus light emitter and absorber for thermophotonic applications. *J. Quant. Spectrosc. Radiat. Transf.* **2022**, *288*, 108271. [CrossRef]
147. Gong, X.; Guan, L.; Li, Q.; Li, Y.; Zhang, T.; Pan, H.; Sun, Q.; Shen, Y.; Grätzel, C.; Zakeeruddin, S.M.; et al. Black phosphorus quantum dots in inorganic perovskite thin films for efficient photovoltaic application. *Sci. Adv.* **2020**, *6*, eaay5661. [CrossRef]
148. Kim, D.K.; Hong, S.B.; Jeong, K.; Lee, C.; Kim, H.; Cho, M.H. P-N Junction Diode Using Plasma Boron-Doped Black Phosphorus for High-Performance Photovoltaic Devices. *ACS Nano* **2019**, *13*, 1683–1693. [CrossRef]
149. Guo, Q.; Pospischil, A.; Bhuiyan, M.; Jiang, H.; Tian, H.; Farmer, D.; Deng, B.; Li, C.; Han, S.J.; Wang, H.; et al. Black phosphorus mid-infrared photodetectors with high gain. *Nano Lett.* **2016**, *16*, 4648–4655. [CrossRef]
150. Xie, C.; Wang, Y.; Zhang, Z.X.; Wang, D.; Luo, L.B. Graphene/Semiconductor Hybrid Heterostructures for Optoelectronic Device Applications. *Nano Today* **2018**, *19*, 41–83. [CrossRef]
151. Yan, F.; Wei, Z.; Wei, X.; Lv, Q.; Zhu, W.; Wang, K. Toward High-Performance Photodetectors Based on 2D Materials: Strategy on Methods. *Small Methods* **2018**, *2*, 1700349. [CrossRef]
152. Zhang, L.; Wang, B.; Zhou, Y.; Wang, C.; Chen, X.; Zhang, H. Synthesis Techniques, Optoelectronic Properties, and Broadband Photodetection of Thin-Film Black Phosphorus. *Adv. Opt. Mater.* **2020**, *8*, 72–81. [CrossRef]
153. Zhou, X.; Hu, X.; Yu, J.; Liu, S.; Shu, Z.; Zhang, Q.; Li, H.; Ma, Y.; Xu, H.; Zhai, T. 2D Layered Material-Based van der Waals Heterostructures for Optoelectronics. *Adv. Funct. Mater.* **2018**, *28*, 1706587. [CrossRef]
154. Yang, Z.; Hao, J. Recent Progress in Black-Phosphorus-Based Heterostructures for Device Applications. *Small Methods* **2018**, *2*, 1700296. [CrossRef]
155. Yuan, J.; Najmaei, S.; Zhang, Z.; Zhang, J.; Lei, S.; Ajayan, P.M.; Yakobson, B.I.; Lou, J. Photoluminescence quenching and charge transfer in artificial heterostacks of monolayer transition metal dichalcogenides and few-layer black phosphorus. *ACS Nano* **2015**, *9*, 555–563. [CrossRef]
156. Huang, H.; Li, J.; Yi, Y.; Wang, J.; Kang, Y.; Chu, P.K.; Ong, H.C.; Yu, X.F. In situ growth of all-inorganic perovskite nanocrystals on black phosphorus nanosheets. *Chem. Commun.* **2018**, *54*, 2365–2368. [CrossRef]
157. Qiao, H.; Li, Z.; Huang, Z.; Ren, X.; Kang, J.; Qiu, M.; Liu, Y.; Qi, X.; Zhong, J.; Zhang, H. Self-powered photodetectors based on 0D/2D mixed dimensional heterojunction with black phosphorus quantum dots as hole accepters. *Appl. Mater. Today* **2020**, *20*, 100765. [CrossRef]
158. Naguib, M.; Kurtoglu, M.; Presser, V.; Lu, J.; Niu, J.; Heon, M.; Hultman, L.; Gogotsi, Y.; Barsoum, M.W. Two-dimensional nanocrystals produced by exfoliation of Ti_3AlC_2. *Adv. Mater.* **2011**, *23*, 4248–4253. [CrossRef]
159. Naguib, M.; Mochalin, V.N.; Barsoum, M.W.; Gogotsi, Y. 25th anniversary article: MXenes: A new family of two-dimensional materials. *Adv. Mater.* **2014**, *26*, 992–1005. [CrossRef]
160. Dhamodharan, D.; Dhinakaran, V.; Byun, H.S. MXenes: An emerging 2D material. *Carbon N. Y.* **2022**, *192*, 366–383. [CrossRef]
161. Anasori, B.; Lukatskaya, M.R.; Gogotsi, Y. 2D metal carbides and nitrides (MXenes) for energy storage. *Nat. Rev. Mater.* **2017**, *2*, 16098. [CrossRef]
162. Zhang, C.J.; Anasori, B.; Seral-Ascaso, A.; Park, S.H.; McEvoy, N.; Shmeliov, A.; Duesberg, G.S.; Coleman, J.N.; Gogotsi, Y.; Nicolosi, V. Transparent, Flexible, and Conductive 2D Titanium Carbide (MXene) Films with High Volumetric Capacitance. *Adv. Mater.* **2017**, *29*, 1702678. [CrossRef] [PubMed]
163. Zhang, C.J.; Nicolosi, V. Graphene and MXene-based transparent conductive electrodes and supercapacitors. *Energy Storage Mater.* **2019**, *16*, 102–125. [CrossRef]

164. Dong, Y.; Chertopalov, S.; Maleski, K.; Anasori, B.; Hu, L.; Bhattacharya, S.; Rao, A.M.; Gogotsi, Y.; Mochalin, V.N.; Podila, R. Saturable Absorption in 2D Ti_3C_2 MXene Thin Films for Passive Photonic Diodes. *Adv. Mater.* **2018**, *30*, 1705714. [CrossRef] [PubMed]
165. Berdiyorov, G.R. Optical properties of functionalized $Ti_3C_2T_2$ (T = F, O, OH) MXene: First-principles calculations. *AIP Adv.* **2016**, *6*, 055105. [CrossRef]
166. Bai, Y.; Zhou, K.; Srikanth, N.; Pang, J.H.L.; He, X.; Wang, R. Dependence of elastic and optical properties on surface terminated groups in two-dimensional MXene monolayers: A first-principles study. *RSC Adv.* **2016**, *6*, 35731–35739. [CrossRef]
167. Xu, Q.; Ding, L.; Wen, Y.; Yang, W.; Zhou, H.; Chen, X.; Street, J.; Zhou, A.; Ong, W.J.; Li, N. High photoluminescence quantum yield of 18.7% by using nitrogen-doped Ti_3C_2 MXene quantum dots. *J. Mater. Chem. C* **2018**, *6*, 6360–6369. [CrossRef]
168. Huang, D.; Xie, Y.; Lu, D.; Wang, Z.; Wang, J.; Yu, H.; Zhang, H. Demonstration of a White Laser with V_2C MXene-Based Quantum Dots. *Adv. Mater.* **2019**, *31*, 1901117. [CrossRef] [PubMed]
169. Hantanasirisakul, K.; Zhao, M.Q.; Urbankowski, P.; Halim, J.; Anasori, B.; Kota, S.; Ren, C.E.; Barsoum, M.W.; Gogotsi, Y. Fabrication of $Ti_3C_2T_x$ MXene Transparent Thin Films with Tunable Optoelectronic Properties. *Adv. Electron. Mater.* **2016**, *2*, 1600050. [CrossRef]
170. Jhon, Y.I.; Koo, J.; Anasori, B.; Seo, M.; Lee, J.H.; Gogotsi, Y.; Jhon, Y.M. Metallic MXene Saturable Absorber for Femtosecond Mode-Locked Lasers. *Adv. Mater.* **2017**, *29*, 1702496. [CrossRef]
171. Jiang, X.; Kuklin, A.V.; Baev, A.; Ge, Y.; Ågren, H.; Zhang, H.; Prasad, P.N. Two-dimensional MXenes: From morphological to optical, electric, and magnetic properties and applications. *Phys. Rep.* **2020**, *848*, 1–58. [CrossRef]
172. Yi, J.; Du, L.; Li, J.; Yang, L.; Hu, L.; Huang, S.; Dong, Y.; Miao, L.; Wen, S.; Mochalin, V.N.; et al. Unleashing the potential of Ti_2CT_x MXene as a pulse modulator for mid-infrared fiber lasers. *2D Mater.* **2019**, *6*, 045038. [CrossRef]
173. Dillon, A.D.; Ghidiu, M.J.; Krick, A.L.; Griggs, J.; May, S.J.; Gogotsi, Y.; Barsoum, M.W.; Fafarman, A.T. Highly Conductive Optical Quality Solution-Processed Films of 2D Titanium Carbide. *Adv. Funct. Mater.* **2016**, *26*, 4162–4168. [CrossRef]
174. Chen, J.; Chen, M.; Zhou, W.; Xu, X.; Liu, B.; Zhang, W.; Wong, C. Simplified Synthesis of Fluoride-Free $Ti_3C_2T_x$ via Electrochemical Etching to Performance Electrochemical Capacitors. *ACS Nano* **2022**, *16*, 2461–2470. [CrossRef] [PubMed]
175. Chertopalov, S.; Mochalin, V.N. Environment-Sensitive Photoresponse of Spontaneously Partially Oxidized Ti_3C_2 MXene Thin Films. *ACS Nano* **2018**, *12*, 6109–6116. [CrossRef] [PubMed]
176. Yu, Z.; Feng, W.; Lu, W.; Li, B.; Yao, H.; Zeng, K.; Ouyang, J. MXenes with tunable work functions and their application as electron- and hole-transport materials in non-fullerene organic solar cells. *J. Mater. Chem. A* **2019**, *7*, 11160–11169. [CrossRef]
177. Agresti, A.; Pazniak, A.; Pescetelli, S.; Di Vito, A.; Rossi, D.; Pecchia, A.; Auf der Maur, M.; Liedl, A.; Larciprete, R.; Kuznetsov, D.V.; et al. Titanium-carbide MXenes for work function and interface engineering in perovskite solar cells. *Nat. Mater.* **2019**, *18*, 1228–1234. [CrossRef]
178. Zhang, J.; Tan, B.; Zhang, X.; Gao, F.; Hu, Y.; Wang, L.; Duan, X.; Yang, Z.; Hu, P.A. Atomically Thin Hexagonal Boron Nitride and Its Heterostructures. *Adv. Mater.* **2021**, *33*, 2000769. [CrossRef] [PubMed]
179. Cassabois, G.; Valvin, P.; Gil, B. Hexagonal boron nitride is an indirect bandgap semiconductor. *Nat. Photonics* **2016**, *10*, 262–266. [CrossRef]
180. Bilal, M.; Xu, W.; Wang, C.; Wen, H.; Zhao, X.; Song, D.; Ding, L. Optoelectronic properties of monolayer hexagonal boron nitride on different substrates measured by Terahertz time-domain spectroscopy. *Nanomaterials* **2020**, *10*, 762. [CrossRef]
181. Tan, B.; Wu, Y.; Gao, F.; Yang, H.; Hu, Y.; Shang, H.; Zhang, X.; Zhang, J.; Li, Z.; Fu, Y.; et al. Engineering the Optoelectronic Properties of 2D Hexagonal Boron Nitride Monolayer Films by Sulfur Substitutional Doping. *ACS Appl. Mater. Interfaces* **2022**, *14*, 16453–16461. [CrossRef] [PubMed]
182. Yamoah, M.A.; Yang, W.; Pop, E.; Goldhaber-Gordon, D. High-Velocity Saturation in Graphene Encapsulated by Hexagonal Boron Nitride. *ACS Nano* **2017**, *11*, 9914–9919. [CrossRef] [PubMed]
183. Meng, J.H.; Liu, X.; Zhang, X.W.; Zhang, Y.; Wang, H.L.; Yin, Z.G.; Zhang, Y.Z.; Liu, H.; You, J.B.; Yan, H. Interface engineering for highly efficient graphene-on-silicon Schottky junction solar cells by introducing a hexagonal boron nitride interlayer. *Nano Energy* **2016**, *28*, 44–50. [CrossRef]
184. Raj, V.; Chugh, D.; Black, L.E.; Shehata, M.M.; Li, L.; Kremer, F.; Macdonald, D.H.; Tan, H.H.; Jagadish, C. Passivation of InP solar cells using large area hexagonal-BN layers. *NPJ 2D Mater. Appl.* **2021**, *5*, 12. [CrossRef]
185. Veeralingam, S.; Durai, L.; Yadav, P.; Badhulika, S. Record-High Responsivity and Detectivity of a Flexible Deep-Ultraviolet Photodetector Based on Solid State-Assisted Synthesized hBN Nanosheets. *ACS Appl. Electron. Mater.* **2021**, *3*, 1162–1169. [CrossRef]
186. Wu, S.C.; Wu, M.J.; Chen, Y.F. Nanolayered Graphene/Hexagonal Boron Nitride/n-AlGaN Heterostructures as Solar-Blind Deep-Ultraviolet Photodetectors. *ACS Appl. Nano Mater.* **2020**, *3*, 7595–7603. [CrossRef]
187. Yuan, S.; Shen, C.; Deng, B.; Chen, X.; Guo, Q.; Ma, Y.; Abbas, A.; Liu, B.; Haiges, R.; Ott, C.; et al. Air-Stable Room-Temperature Mid-Infrared Photodetectors Based on hBN/Black Arsenic Phosphorus/hBN Heterostructures. *Nano Lett.* **2018**, *18*, 3172–3179. [CrossRef] [PubMed]
188. Cho, A.J.; Kwon, J.Y. Hexagonal Boron Nitride for Surface Passivation of Two-Dimensional van der Waals Heterojunction Solar Cells. *ACS Appl. Mater. Interfaces* **2019**, *11*, 39765–39771. [CrossRef]
189. Wang, Y.; Ren, B.; Qu, J.Z.; Xu, K.; Yang, C.; Li, Y.; Zhang, H. Engineering two-dimensional metal oxides and chalcogenides for enhanced electro- and photocatalysis. *Sci. Bull.* **2021**, *66*, 1228–1252. [CrossRef]

190. Kumbhakar, P.; Chowde Gowda, C.; Mahapatra, P.L.; Mukherjee, M.; Malviya, K.D.; Chaker, M.; Chandra, A.; Lahiri, B.; Ajayan, P.M.; Jariwala, D.; et al. Emerging 2D metal oxides and their applications. *Mater. Today* **2021**, *45*, 142–168. [CrossRef]
191. Hu, X.; Liu, K.; Cai, Y.; Zang, S.-Q.; Zhai, T. 2D Oxides for Electronics and Optoelectronics. *Small Sci.* 2022; *early view*. [CrossRef]
192. Yu, H.; Liao, Q.; Kang, Z.; Wang, Z.; Liu, B.; Zhang, X.; Du, J.; Ou, Y.; Hong, M.; Xiao, J.; et al. Atomic-Thin ZnO Sheet for Visible-Blind Ultraviolet Photodetection. *Small* **2020**, *16*, 2005520. [CrossRef]
193. Messalea, K.A.; Carey, B.J.; Jannat, A.; Syed, N.; Mohiuddin, M.; Zhang, B.Y.; Zavabeti, A.; Ahmed, T.; Mahmood, N.; Della Gaspera, E.; et al. Bi_2O_3 monolayers from elemental liquid bismuth. *Nanoscale* **2018**, *10*, 15615–15623. [CrossRef]
194. Yin, C.; Gong, C.; Chu, J.; Wang, X.; Yan, C.; Qian, S.; Wang, Y.; Rao, G.; Wang, H.; Liu, Y.; et al. Ultrabroadband Photodetectors up to 10.6 μm Based on 2D Fe_3O_4 Nanosheets. *Adv. Mater.* **2020**, *32*, 4–11. [CrossRef] [PubMed]
195. Zhong, M.; Zhou, K.; Wei, Z.; Li, Y.; Li, T.; Dong, H.; Jiang, L.; Li, J.; Hu, W. Highly anisotropic solar-blind UV photodetector based on large-size two-dimensional α-MoO_3 atomic crystals. *2D Mater.* **2018**, *5*, 035033. [CrossRef]
196. Chen, Q.; Zhang, Y.; Zheng, T.; Liu, Z.; Wu, L.; Wang, Z.; Li, J. Polarization detection in deep-ultraviolet light with monoclinic gallium oxide nanobelts. *Nanoscale Adv.* **2020**, *2*, 2705–2712. [CrossRef]
197. Zheng, W.; Lin, R.; Zhu, Y.; Zhang, Z.; Ji, X.; Huang, F. Vacuum Ultraviolet Photodetection in Two-Dimensional Oxides. *ACS Appl. Mater. Interfaces* **2018**, *10*, 20696–20702. [CrossRef] [PubMed]
198. Geim, A.K.; Grigorieva, I.V. Van der Waals heterostructures. *Nature* **2013**, *499*, 419–425. [CrossRef] [PubMed]
199. Guo, P.; Xu, J.; Gong, K.; Shen, X.; Lu, Y.; Qiu, Y.; Xu, J.; Zou, Z.; Wang, C.; Yan, H.; et al. On-Nanowire Axial Heterojunction Design for High-Performance Photodetectors. *ACS Nano* **2016**, *10*, 8474–8481. [CrossRef]
200. Kretinin, A.V.; Cao, Y.; Tu, J.S.; Yu, G.L.; Jalil, R.; Novoselov, K.S.; Haigh, S.J.; Gholinia, A.; Mishchenko, A.; Lozada, M.; et al. Electronic properties of graphene encapsulated with different two-dimensional atomic crystals. *Nano Lett.* **2014**, *14*, 3270–3276. [CrossRef]
201. Dean, C.R.; Young, A.F.; Meric, I.; Lee, C.; Wang, L.; Sorgenfrei, S.; Watanabe, K.; Taniguchi, T.; Kim, P.; Shepard, K.L.; et al. Boron nitride substrates for high-quality graphene electronics. *Nat. Nanotechnol.* **2010**, *5*, 722–726. [CrossRef]
202. Liao, W.; Huang, Y.; Wang, H.; Zhang, H. Van der Waals heterostructures for optoelectronics: Progress and prospects. *Appl. Mater. Today* **2019**, *16*, 435–455. [CrossRef]
203. Ren, K.; Sun, M.L.; Luo, Y.; Wang, S.K.; Yu, J.; Tang, W.C. First-principle study of electronic and optical properties of two-dimensional materials-based heterostructures based on transition metal dichalcogenides and boron phosphide. *Appl. Surf. Sci.* **2019**, *476*, 70–75. [CrossRef]
204. Shu, H. Structural stability, tunable electronic and optical properties of two-dimensional WS_2 and GaN heterostructure: First-principles calculations. *Mater. Sci. Eng. B Solid-State Mater. Adv. Technol.* **2020**, *261*, 114672. [CrossRef]
205. Yang, X.; Wu, R.; Zheng, B.; Luo, Z.; You, W.; Liu, H.; Li, L.; Zhang, Y.; Tan, Q.; Liang, D.; et al. A Waveguide-Integrated Two-Dimensional Light-Emitting Diode Based on p-Type WSe_2/n-Type CdS Nanoribbon Heterojunction. *ACS Nano* **2022**, *16*, 4371–4378. [CrossRef] [PubMed]
206. Shang, H.; Chen, H.; Dai, M.; Hu, Y.; Gao, F.; Yang, H.; Xu, B.; Zhang, S.; Tan, B.; Zhang, X.; et al. A mixed-dimensional 1D Se-2D InSe van der Waals heterojunction for high responsivity self-powered photodetectors. *Nanoscale Horiz.* **2020**, *5*, 564–572. [CrossRef]
207. Geng, H.; Yuan, D.; Yang, Z.; Tang, Z.; Zhang, X.; Yang, K.; Su, Y. Graphene van der Waals heterostructures for high-performance photodetectors. *J. Mater. Chem. C* **2019**, *7*, 11056–11067. [CrossRef]
208. Chen, Y.; Wang, Y.; Wang, Z.; Gu, Y.; Ye, Y.; Chai, X.; Ye, J.; Chen, Y.; Xie, R.; Zhou, Y.; et al. Unipolar barrier photodetectors based on van der Waals heterostructures. *Nat. Electron.* **2021**, *4*, 357–363. [CrossRef]
209. Paul, K.K.; Kim, J.H.; Lee, Y.H. Hot carrier photovoltaics in van der Waals heterostructures. *Nat. Rev. Phys.* **2021**, *3*, 178–192. [CrossRef]
210. Zhou, H.; Lai, H.; Sun, X.; Zhang, N.; Wang, Y.; Liu, P.; Zhou, Y.; Xie, W. Van der Waals MoS_2/Two-Dimensional Perovskite Heterostructure for Sensitive and Ultrafast Sub-Band-Gap Photodetection. *ACS Appl. Mater. Interfaces* **2022**, *14*, 3356–3362. [CrossRef]
211. Guo, Y.; Min, J.; Cai, X.; Zhang, L.; Liu, C.; Jia, Y. Two-Dimensional Type-II BP/$MoSi_2P_4$vdW Heterostructures for High-Performance Solar Cells. *J. Phys. Chem. C* **2022**, *126*, 4677–4683. [CrossRef]
212. Lv, Q.; Yan, F.; Wei, X.; Wang, K. High-Performance, Self-Driven Photodetector Based on Graphene Sandwiched GaSe/WS_2 Heterojunction. *Adv. Opt. Mater.* **2018**, *6*, 2–7. [CrossRef]
213. Wu, E.; Wu, D.; Jia, C.; Wang, Y.; Yuan, H.; Zeng, L.; Xu, T.; Shi, Z.; Tian, Y.; Li, X. In Situ Fabrication of 2D WS_2/Si Type-II Heterojunction for Self-Powered Broadband Photodetector with Response up to Mid-Infrared. *ACS Photonics* **2019**, *6*, 565–572. [CrossRef]
214. Zhong, J.; Wu, B.; Madoune, Y.; Wang, Y.; Liu, Z.; Liu, Y. $PdSe_2$/$MoSe_2$ vertical heterojunction for self-powered photodetector with high performance. *Nano Res.* **2022**, *15*, 2489–2496. [CrossRef]
215. Cao, G.; Wang, F.; Peng, M.; Shao, X.; Yang, B.; Hu, W.; Li, X.; Chen, J.; Shan, Y.; Wu, P.; et al. Multicolor Broadband and Fast Photodetector Based on InGaAs–Insulator–Graphene Hybrid Heterostructure. *Adv. Electron. Mater.* **2020**, *6*, 1901007. [CrossRef]
216. Jiang, W.; Zheng, T.; Wu, B.; Jiao, H.; Wang, X.; Chen, Y.; Zhang, X.; Peng, M.; Wang, H.; Lin, T.; et al. A versatile photodetector assisted by photovoltaic and bolometric effects. *Light Sci. Appl.* **2020**, *9*, 160. [CrossRef] [PubMed]